TABLE 1   Diffusion constants of monomeric EGFP and tandem $EGFP_n$ in the cytoplasm, the nucleoplasm, and the nucleolus in three different living cells (23)

		Fast (fraction)		Slow (fraction)	Very slow (fraction)
*Fast-diffusion-mobility (Cyt and NP)		(>90%)		–	(<10%)
Slow-diffusion-mobility (NL)		(<80%)		(20%~100%)	–
		Cyt (fast/first components)		NP (fast/first components)	
†Cell line	Type of GFP	D ($\mu m^2 s^{-1}$)	Fraction (%)	D ($\mu m^2 s^{-1}$)	Fraction (%)
HeLa	GFP_1	23.4 ± 2.5	95	22.7 ± 2.3	96
	GFP_2	16.4 ± 0.8	92	14.9 ± 0.8	93
	GFP_3	13.1 ± 1.4	91	11.6 ± 1.7	91
	GFP_4	9.0 ± 0.8	93	8.6 ± 0.6	90
	GFP_5	8.3 ± 1.1	90	7.8 ± 1.2	90
COS7	GFP_1	27.1 ± 3.0	90	22.3 ± 1.3	95
	GFP_2	15.8 ± 1.0	93	14.9 ± 0.3	92
	GFP_3	14.7 ± 0.6	91	11.1 ± 0.8	94
	GFP_4	10.8 ± 1.0	92	9.2 ± 0.8	91
	GFP_5	9.5 ± 1.0	90	7.9 ± 0.4	90
HEK	GFP_1	21.0 ± 1.6	95	24.9 ± 2.1	93
	GFP_2	17.4 ± 3.5	92	16.4 ± 2.2	95
	GFP_3	14.1 ± 1.4	91	13.2 ± 0.9	91
	GFP_4	10.3 ± 1.1	90	10.5 ± 1.8	90
	GFP_5	10.4 ± 0.5	92	9.6 ± 0.4	92
		NL (fast/first components)		NL (slow/second components)	
Cell line	Type of GFP	$D^{\ddagger}$ ($\mu m^2 s^{-1}$)	Fraction (%)	$D^{\ddagger}$ ($\mu m^2 s^{-1}$)	Fraction (%)
HeLa	GFP_1	24.2 ± 1.3	–	5.8 ± 1.6	–
	GFP_2	17.6 ± 1.2	–	3.8 ± 0.5	–
	GFP_3	13.0 ± 1.0	–	2.1 ± 0.3	–
	GFP_4	11.0 ± 0.7	–	1.9 ± 0.1	–
	GFP_5	8.9 ± 0.4	–	1.6 ± 0.4	–
COS7	GFP_1	22.8 ± 1.7	–	5.7 ± 1.6	–
	GFP_2	16.1 ± 2.9	–	3.7 ± 0.8	–
	GFP_3	13.3 ± 1.5	–	1.7 ± 0.2	–
	GFP_4	9.0 ± 0.3	–	1.3 ± 0.2	–
	GFP_5	9.1 ± 0.8	–	1.1 ± 0.2	–

*Two kinds of mobility, fast-diffusion-mobility and slow-diffusion-mobility, were differentiated by two-component analysis of G (τ). The fast-diffusion-mobility has "fast" and "very slow" components. In contrast, the slow-diffusion-mobility has "fast" and "slow" components. These three components have different ranges for the diffusion time and fraction.

†The diffusion constants and fractions in cytoplasm (Cyt) and nucleoplasm (NP) correspond to the average diffusion constants and fractions for the first component of the fast-diffusion-mobility ("fast" in top part of table). The diffusion constant and fractions of the second component ("very slow" in top part of table) is not shown. The diffusion constant in the nucleolus (NL) corresponds to those for the first component ("fast" in top part of table) and the second component ("slow" in top part of table) of the slow-diffusion-mobility. The fraction in the NL was not shown because the values were very variable (see also the text). The values of D in NL indicated those having a fraction >50%. Data were averaged over 15–20 cells for HeLa, COS7, and HEK293 (Mean ± SE of three independent experiments).

‡The average values of D in the nucleolus were obtained from cells only expressing monomer EGFP and tandem $EGFP_n$ without mRFP-fibrillarin. These values were consistent with the result of Fig.5 E obtained by coexpressed cells.

down free diffusion. With conditions of cells having a concentration under 20 $EGFP_n$ molecules (<0.1 μM) and a comparatively short measurement time under 30 s, the influence of photobleaching on diffusion time, which gives rise to a very long diffusion time and an increase of the fraction (y_i value in Eq. 2), could be minimized. Photobleaching effects were checked from the time trace of fluorescent intensity for all FCS data (supplementary Fig. S3). Increasing the incubation time after transfection for a few days made the effect of photobleach on FCS measurement much stronger, because the promoter for protein expression

is strong and not a controlled one. In practice, photobleaching effect was very small for weakly fluorescent cells at an early stage after expression of tandem GFP (supplementary Fig. S4). Background fluorescent signals under 2 × 10^3 cps and 10 × 10^3 cps were detected in medium and nontransfected HeLa, HEK, and COS7 cells (14). No significant correlation amplitudes were detected in the culture medium. In contrast, very weak correlations with very long diffusion times above 10^5 μs were sometimes detected in each cell type when FCS measurement was carried out over longer duration over 60 s. This was derived from very slow

and large fluctuation of fluorescence but not from photo-bleaching. To solve the background with very slow fluctuation, we adapted a shorter measurement time as described above. Considering each tandem EGFP has much larger brightness per molecule than that of monomer EGFP (C. Pack and M. Kinjo, unpublished data) and the diffusion time of the proteins was an order of millisecond ranges, the short measurement time of FCS might be enough to obtain a reliable autocorrelation function.

Two diffusional mobility in the nucleus

The fast-diffusion-mobility in the cytoplasm and the nucleus

Fig. 4 A shows a plot of the diffusion time of first component obtained from FAFs representing the fast-diffusion-mobility in the cytoplasm and in the nucleus of HeLa cells (curves 1 and 2 in Fig. 3, B, D, and F). For these FAFs of the fast-diffusion-mobility, >90% of the fraction (y_1 in Eq. 2) was defined as the first component, which represents free diffusion. These results were highly reproducible. As shown in Fig. 4 A (solid circles), the diffusion times of the fast-diffusion-mobility in the nucleus were gradually increased with the increase in the molecular size of tandem EGFP$_n$. In the cytoplasm (Fig. 4 A, open circles), the diffusion time of the first component for EGFP$_n$ also increased with size. No significant difference between the first components in the cytoplasm and nucleus was found. Average diffusion times of monomeric and oligomeric EGFP in HEK and COS7 cells also increased with increasing the size both in the cytoplasm and in the nucleus (Fig. 4, B and C). The ratio of the diffusion

time of the first component in the cytoplasm and the nucleus of each cell type to that in aqueous solution ($DT_{cell}/DT_{sol.}$), which indicates the ratio of viscosity (Eqs. 3 and 4), is shown in inserts in Fig. 4, A, B and C, respectively. Regardless of the cell type, the average ratios of viscosities in the cytoplasm and the nucleus were not significantly different and 3.5-fold higher than that in solution. Moreover, there was no dependency of the viscosity ratio on the size of oligomeric EGFP$_n$. These results agreed with previous results obtained from microinjected fluorescent macromoleucules and monomeric EGFP (7,13,42).

Using the result that the average viscosity in the cytoplasm and nucleus was 3.5-fold higher than that in solution, the expected diffusion times of tandem EGFP$_n$ in the cell were calculated. As shown in Fig. 2, the measured diffusion times of first components in living cells were also compared with three calculated diffusion times (Fig. 4, A, B, and C) assuming the shape of oligomeric EGFP to be spherical (dashed lines) or rod-like with the expected linker lengths of 4 nm (solid lines) and 9 nm (dotted lines). Dependency of the diffusion times on the size of oligomeric EGFP both in the cytoplasm and in the nucleus was consistent with that of a rod-like molecule rather than a spherical one (dashed lines). Based on the result that the diffusion properties of rod-like molecules of oligomeric EGFP in the cytoplasm and the nucleus are equivalent and consistent with the result in aqueous solution, the oligomeric EGFP$_n$ located in the nucleus was not truncated or degraded. Consequently, our results suggested that the diffusion of oligomeric EGFP$_n$ as a rod-like molecule was well conserved in the cellular circumstance in all of three cell lines.
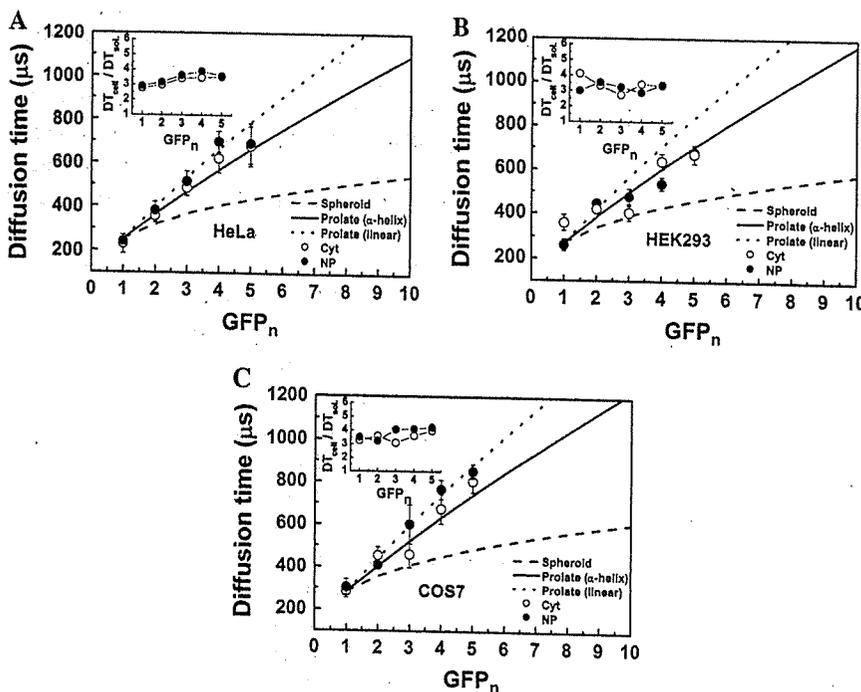

FIGURE 4 Fast diffusional mobility of tandem EGFP$_n$ is dependent on the molecular length. FAFs were fitted with a two-component model using Eq. 2, $i = 2$ for analyzing the diffusion times and the fractions of components 1 and 2. For the FAFs of the fast-diffusion-mobility in Fig. 3 G, the fraction of the first component was >90% for EGFP and tandem EGFP$_n$ in the cytoplasm and the nucleus. The diffusion times of the first components in HeLa cells (A), HEK cells (B), and COS7 cells (C) are plotted. The plots of measured diffusion times shown in panels A, B, and C show the average values of five cells for each protein. The error bars represent mean ± SD. The diffusion times of the first components were increased according to the molecular weight. As shown in Fig. 2, the calculated diffusion times for a spherical and a rod-like molecule were plotted for comparison. Dashed line shows diffusion times calculated by Eq. 5 using the molecular weight and the measured diffusion time of Rh6G assuming the oligomeric EGFP$_n$ are spherical. Solid and dotted lines show the calculated diffusion times assuming that the linker between EGFP forms a rigid α-helix and a linear shape, respectively. Inserts show the ratio of diffusion times of the first component in the cytoplasm and the nucleus to that in aqueous solution.

Other diffusion times (second component) of the FAFs for the fast-diffusion-mobility (curves 1 and 2 in Fig. 3, B, D, and F) were very slow, and ranged from 10^4 to 10^5 μs in the nucleus as well as in the cytoplasm. The range of these long diffusion times was very broad and so it is not clear that the diffusion time of the second component was also dependent on the size of tandem $EGFP_n$. The fraction of the second component (y_2 in Eq. 2) was very small (<10%), regardless of the size of tandem $EGFP_n$. The slow drift of fluorescence could come from cell mobility or very large organelles such as vesicles in cytoplasm (24,42) and such as a compact structure of chromatin in nucleus (4) during FCS measurement. Otherwise very weak photobleaching might be not completely excluded, even though data of photobleached samples were checked and excluded. However, a possibility of trapped diffusion in complex chromatin structures cannot be completely excluded. To analyze an effect of chromatin structures on the very slow diffusion time, we treated cells coexpressing tandem $EGFP_3$ and H2B-mRFP or $EGFP_5$ and H2B-mRFP, respectively, with Trichostatin A (TSA) (supplementary Fig. S5). It was previously reported that TSA inhibits histone deacetylation and so increases chromatin accessibility of relatively larger dextrans (4,43). In LSM observation, no significant changes of fluorescent pattern for tandem $EGFP_3$ and $EGFP_5$ were found, although that of H2B-mRFP was significantly changed after TSA treatment (supplementary Figs. S1 and S5). This result suggests that tandem $EGFP_n$ can freely and equally access to all regions of euchromatin and heterochromatin and so no effect of TSA treatment occurred. Moreover, there were no significant changes of diffusion time and fraction for the very slow component in the nucleoplasm after TSA treatment when FCS measurements on euchromatin (dilute H2B-mRFP fluorescent region) and heterochromatin (dense H2B-mRFP fluorescent region) were carried out (C. Pack and M. Kinjo, unpublished data). Because the fraction of the very slow component was very small (<10%) and the diffusion times were very broad with large standard deviation even before TSA treatment, it is likely that the effect of TSA treatment on mobility of tandem $EGFP_n$ in the nucleus cannot be detectable in our experimental system. Nevertheless, the result of LSM observation was consistent with the result of FCS measurement. Details and discussion of such very slow diffusion can be omitted in this article because the fraction is small and we focus on well-defined diffusion property of tandem $EGFP_n$ as molecular ruler.

The slow-diffusion-mobility in the nucleus

On the other hand, the right-shifted FAFs for tandem $EGFP_n$, which represent the slow diffusion-mobility, found in the nucleus (curves 3, dashed lines in Fig. 3, B, D, and F) showed a different range of diffusion times and a different fraction for the second component compared to those for the fast-diffusion-mobility (curves 1 and 2, solid and dotted lines

in Fig. 3, B, D, and F). Obviously, although the diffusion times of the first component for the slow-diffusion-mobility in the nucleus were consistent with those for the fast-diffusion-mobility in the cytoplasm and in the nucleus (Table 1), the diffusion times of the second component for the slow-diffusion-mobility ranged from 800 to 5000 μs, increasing with the size of tandem EGFP (e.g., curve 3 in Fig. 3, B, D, and F). Moreover, the fraction of the second component for the slow-diffusion-mobility varied from 20 to 100% depending on the cells, and even the measured position in the same nucleus. This observation was very reproducible, and was consistent among the three cell types. Obviously, our results indicated that the protein mobility in the nuclear microenvironment might be separated into two kinds of diffusing species (i.e., the first component of fast-diffusion-mobility and the second component of slow-diffusion-mobility). These two kinds of diffusing species had different ranges of diffusion time (or apparent viscosity) depending on the position inside the nucleus.

The slow-diffusion-mobility of tandem $EGFP_n$ in the nucleolus

Fluorescent intensity at the position of the slow-diffusion-mobility (i.e., the right-shifted FAFs) in the nucleus (position 3 of Fig. 3, A, C, and E) was weak compared to other places inside the nucleus. In addition, the slow-diffusion-mobility was often found in the nucleolus in the cells expressing $EGFP_4$ and $EGFP_5$ with large and clear nucleoli. The density, the number, and the morphology of the nucleolus changed according to the cell cycle as well as cell type and other cell conditions. Recently, the nucleolus has been detected by fluorescence microscopy in cell lines expressing fluorescent protein-tagged nucleolar proteins such as fibrillarin and B23 (32,44). Fibrillarin is related to various steps of pre-rRNA processing and ribosome assembly and located in the dense fibrillar component (DFC) of the nucleolus during interphase (45). Using a nucleolar protein tagged with different fluorescent proteins will help in discriminating the nucleolar structures from nucleoplasm and tracing the changes of the nuclear structure during the cell cycle or depending on physiological cell conditions.

Fig. 5 shows an LSM image and FCS measurement of a HeLa cell coexpressing $EGFP_4$ and mRFP-fibrillarin. The strong red fluorescence in the nucleus (Fig. 5 A) indicates the nucleolus. A weak green fluorescence signal was also detected in the nucleoplasm (Fig. 5 B). This LSM observation for fibrillarin agreed with the previous results (12,32). The shape, the size, and the number of nucleoli were different from cell to cell. Using cotransfected HeLa cells, FCS measurement was carried out for positions of green fluorescent nucleoplasm and the red fluorescent nucleolus with a diameter of over 2 μm in the x-y plane of the LSM image. FAF inside the nucleolus (Fig. 5 D, red line) shifted to the right compared to that in the nucleoplasm (Fig. 5 D, black line), which meant that the diffusion in the nucleolus was
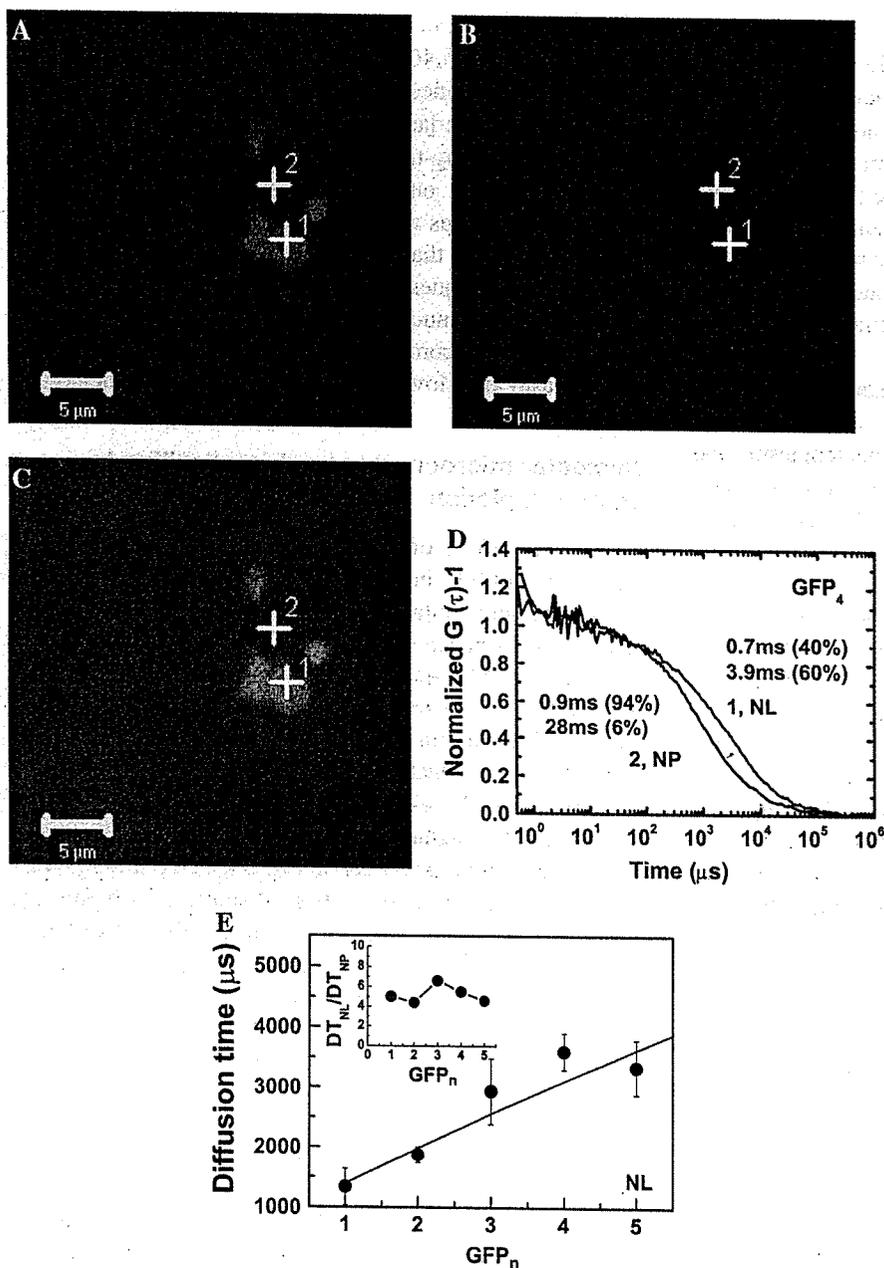
FIGURE 5 Slow diffusional mobility of oligomeric EGFP found in the nucleolus is much slower than that in the nucleoplasm. For clear discrimination of nucleoplasm from nucleolus in cells weakly expressing EGFP and tandem EGFPn, a nucleolar protein of mRFP-fibrillarin was coexpressed. (A) LSM images of HeLa cells coexpressing mRFP-fibrillarin and (B) tetrameric EGFP, and (C) a merged image are shown. Bars, 5 μm. FCS measurement was carried at 24h after cotransfection of genes encoding mRFP-fibrillarin and EGFPn. Nucleoli with a diameter of over 2 μm were selected for FCS measurement. FCS measurements were performed on multiple places in the nucleoplasm and the nucleolus. For clarification, (D) two normalized FAFs (G (0) − 1 = 1) of EGFP4 measured on two points in the nucleoplasm (black curve) and the nucleolus (solid curve) of a single cell are shown. The normalized FAF indicated that the diffusion in the two positions was clearly different. The error bars represent mean ± SD for three measurements of a single cell. (E) The diffusion times of the second components (solid circles) for EGFP and tandem EGFPn in the nucleoli in HeLa cells are plotted. The insert shows the ratio of diffusion time in the nucleolus to that in the nucleoplasm (DT_{NL}/DT_{NP}). Solid line shows the calculated diffusion time using the rod-like model (with an α-helix linker) assuming that the apparent viscosity of the nucleolus is 5.2-fold higher than the nucleoplasm (insert). The plots of measured diffusion times shown in panel E represent the average values of six cells for each protein. The error bars represent mean ± SE. (NP, nucleoplasm; NL, nucleolus.)

much slower than that in the nucleoplasm. The FAFs obtained from nucleolus fit well with the two-component model. Occasionally, some FAFs fit well even in the one-component model. The slow-diffusion-mobility in the nucleolus (Fig. 5 D; curve 1) consisted of the first component of 700 μs (40%) and the second component of 3900 μs (60%). In contrast, the fast-diffusion-mobility in the nucleoplasm (Fig. 5 D; curve 2) consisted of the first component of 900 μs (94%) and the second component of 28,000 μs (6%). Diffusion times (1 × 10^3–4 × 10^3 μs) of second components for FAFs measured in the nucleolus (Fig. 5 E) were much shorter than those of second components measured in the nucleoplasm and the cytoplasm (ranging from 10^4 to 10^5 μs). The time range (Fig. 5 E) was consistent with

those obtained from Fig. 3, B, D, and F. In contrast, almost no such diffusional component in the range of 1 × 10^3–4 × 10^3 μs was found in places other than the nucleolus. On the other hand, the diffusion time of the first component in the nucleolus was the same as those in the cytoplasm and the nucleoplasm. The fraction of the first component was decreased with the increased fraction of the second component. The diffusion times of second components in the nucleoli increased with the size of EGFP1, EGFP2, EGFP3, and EGFP4, even though there was little difference between EGFP4 and EGFP5 (solid circles in Fig. 5 E). The inset in Fig. 5 E shows the average ratio of the diffusion time of the second component in the nucleolus to the diffusion time of the first component in the nucleoplasm (DT_{NL}/DT_{NP}). There

was no dependency of the ratio on the size of EGFP$_n$ and average value of the ratio for all tandem EGFP$_n$ was ~5.2. The solid line in Fig. 5 E shows the calculated diffusion times of tandem EGFP$_n$ as a rod-like molecule with an α-helix linker when the relative viscosity in the nucleolus is fixed by the average ratio of diffusion time (Fig. 5 E, inset). The measured diffusion times of tandem EGFP$_n$ were consistent with the calculated values. Our results indicated that the slow-diffusion-mobility in the nucleolus also reflected the diffusion of a rod-like molecule rather than a spherical molecule.

Table 1 summarizes the diffusion constants of the fast-diffusion-mobility (the first component with a fraction >90%) found in the cytoplasm and the nucleoplasm, and the diffusion constants of the slow-diffusion-mobility (first and second components) found in the nucleolus. The average values were obtained from living cells only expressing monomer EGFP and tandem EGFP$_n$ without mRFP-fibrillarin. Diffusion constants of the fast-diffusion-mobility both in the nucleoplasm and in the cytoplasm decreased with the length of tandem EGFP$_n$ in HeLa, COS7, and HEK cells, even though the diffusion constants of EGFP$_4$ and EGFP$_5$ in the cytoplasm of HEK cells did not change. Diffusion constants of the first and the second components in the nucleoli of HeLa and COS7 cells also decreased with the length of EGFP$_n$. There was little difference between diffusion constants in the cytoplasm and the nucleoplasm of HEK293 and HeLa cells. In contrast, diffusion constants in the cytoplasm of COS7 cells were slightly larger than those in the nucleoplasm. Based on these results, it was concluded that the diffusional motion of tandem EGFP$_n$ in the nucleous as well as in the cytoplasm and the nucleoplasm was well consistent with free diffusion of rod-like molecules, regardless of the cell type. It is emphasized that the microenvironment of the nucleolus as well as the nucleoplasm and the cytoplasm could be quantitatively understood by diffusion analysis of the oligomeric EGFP$_n$ as molecular rulers (MR). Moreover, our results indicated that the microenvironment and apparent viscosity of the cytoplasm and the nucleoplasm were almost same, even though the constituents of the two compartments were very different.

Compared with those of the first component in the nucleoplasm, the fractions of the second components in the nucleoli were significantly changed from 20 to 100% depending on the nucleolus, even in the same cell (C. Pack and M. Kinjo, unpublished data). Because the length of the z axis (optical axis) of detection volume (<2 μm) was six times longer than the diameter in the x-y plane (<0.2 μm), FCS measurement of a nucleolus with a length in the z axis shorter than 2 μm might contain both the nucleoplasm and the nucleolus. This might affect the variability of the fraction. However, it is also presumed that the diffusion of oligomeric EGFP$_n$ in the nucleolus has more variability than that found in the cytoplasm and the nucleoplasm, indicating the dynamic change of the nucleolar microenvironment or the complexity of subnu-

cleolar structures such as DFC, fibrillar centers, and the granular region (45,46). More detailed study using two-color 3D imaging combined with FCS measurement is in progress for elucidating the large diffusion changes in the nucleolus according to a long-time scale or the cell cycle of a single cell. Nevertheless, our results showed that the mobility of MR in the nucleolus was dependent onto length of them, but was much slower than those in the cytoplasm and the nucleoplasm. Consequently, it was concluded that the diffusion of protein in the nucleus must be separated into two significant diffusing components, fast-diffusion-mobility in the nucleoplasm and slow-diffusion-mobility in the nucleolus.

Nucleolar microenvironment is sensitive to energy depletion

To examine effect of energy depletion on the mobility of oligomeric EGFP in the nuclear microenvironment, the culture medium containing HeLa cells expressing EGFP$_4$ or EGFP$_5$ was perfused with 2-DG and NaN$_3$ solution (3,20) at 25 or 37°C. LSM and FCS measurements were carried out with HeLa cells expressing EGFP$_5$ or coexpressing EGFP$_5$ and mRFP-fibrillarin (or H2B-mRFP). For FCS measurement of cells transfected with EGFP$_5$, HeLa cells with clear and large nucleoli (>4 μm in diameter) were chosen despite the fluorescence signals of the cytoplasm being a little strong (for example, right upper cell in Fig. 3 E). FCS measurement was carried on the same position of single cells before and after the energy depletion. We confirmed the redistribution of H2B-mRFP and nuclear shrinkage through LSM images of cells coexpressing H2B-mRFP and EGFP$_5$ after ATP depletion at room temperature for 30 min (C. Pack and M. Kinjo, unpublished data). This result was consistent with a previous study (20). With cells expressing EGFP$_5$, Fig. 6, A–C, show FAFs of EGFP$_5$ at the same positions in the cytoplasm, the nucleoplasm, and the nucleolus of a single HeLa cell, respectively, before (dashed black lines) and after the energy depletion (solid red lines). FAFs of EGFP$_5$ both in the cytoplasm and in the nucleoplasm were slightly shifted to the right by the energy depletion (Fig. 6, A and B). In contrast, the FAF of EGFP$_5$ in the nucleolus was significantly changed in the longer time range as shown in Fig. 6 C. The energy depletion induced a big tail on the FAF, which indicates that a fraction with much slower mobility was newly produced. The diffusion time corresponding to the tail found in the nucleolus was 13-fold slower than that of the second component found before energy depletion, and the fraction of the new slower component was increased from 0% up to ~32% (Fig. 6 C).

Fig. 6, D–F, shows the average change of the diffusion time and the fraction in each cellular compartment of five HeLa cells expressing EGFP$_5$. Averaged diffusion times in the cytoplasm (0.8 ± 0.04 ms and 0.85 ± 0.04 ms) and the nucleoplasm (0.79 ± 0.06 ms and 0.7 ± 0.08 ms) before and after ATP depletion, respectively, were not changed (solid
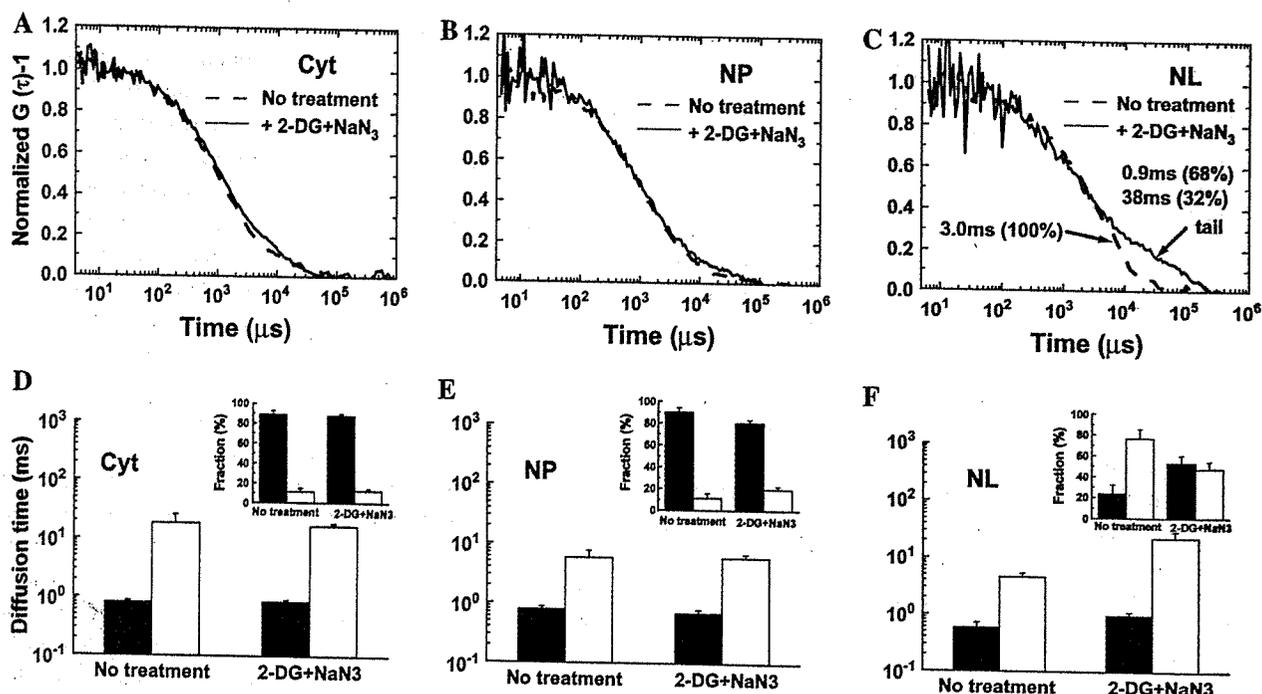
FIGURE 6   MR mobility in the nucleolus is changed by the energy depletion. HeLa cells were transiently transfected with EGFP5, or cotransfected with EGFP5 and H2B-mRFP. The FAF of EGFP5 in single HeLa cells is shown before (dashed black lines) and 30 min after addition (solid red lines) of 2-deoxyglucose (6 mM) and sodium-azide (10 mM) to culture medium at room temperature. The redistribution of H2B-mRFP on the cells coexpressed with EGFP5 was confirmed by LSM before and after the treatment. The changes of the normalized FAF on (A) cytoplasm, (B) nucleoplasm, and (C) nucleolus of a single cell induced by energy depletion are shown. The amplitude of FAF, $G(0) - 1$, was normalized to unity. The average diffusion times and the average fractions (insert) of the first (solid bars) and the second (open bars) components for EGFP5 in the cytoplasm, the nucleoplasm, and the nucleolus before and after ATP depletion are shown in panels D, E, and F, respectively. The error bars are the measured mean $\pm$ SE ($n = 8$ cells).

bars in Fig. 6, D and E). Instead, the fractions of first components were slightly decreased in the cytoplasm (~1%) and the nucleoplasm (~9%) (Fig. 6, D and E, solid bars in inset). On the other hand, diffusion times of the second component in the nucleolus were increased from 4.6 $\pm$ 0.8ms to 22.4 $\pm$ 6.7 ms (Fig. 6 F, open bars), even though the fraction of the second component was decreased from 77 to 47% by the energy depletion (Fig. 6 F, open bars in inset). In addition to the change of the second component in the nucleolus, the diffusion time of the first component in the nucleolus was also increased from 0.58 $\pm$ 0.1 ms to 1.0 $\pm$ 0.1 ms (Fig. 6 F, solid bars). This indicated that the microenvironment inside the nucleolus, which was reflected by diffusion of EGFP5 molecules, was more sensitive to energy depletion than those of the nucleoplasm and the cytoplasm.

DISCUSSION

Tandemly linked EGFPn proteins were constructed for modeling rod-like molecules. The diffusion properties of the proteins were quantitatively dependent on their length. These series of standard proteins allowed us to analyze protein mobility in living cells. LSM observation of HeLa cells expressing monomer EGFP and four different kinds of tandem EGFPn showed that the proteins could be distributed to the cell nucleus regardless of their molecular weights. Mono-

meric EGFP, EGFP2, and EGFP3 were easily distributed in the nucleus. In contrast, the fluorescent intensities in the nuclei of cells expressing EGFP4 and EGFP5 were lower than in the cytoplasm, even though they were also located in the cell nuclei. Although the tendency of fluorescence intensity was very much different for EGFPn in the nucleus, all tandem proteins were detected by LSM and could also be detected by FCS. Many studies have shown that the transport of inert molecules to the nucleus depends inversely on molecular size with an exclusion limit at ~5–10 nm in diameter or 40–60 kD in molecular weight (47,48). These studies discussed only the exclusion limits of spherical molecules. Our results for tandem EGFPn with molecular weights of 60, 90, 120, and 150 kD showed that rod-like proteins could localize to the cell nucleus within 24h after transfection depending on size, even though the mechanism for their transport to the nucleus was not clear.

Western blots of tandem proteins from cell lysates showed that the molecular weights of proteins synthesized in cells were well consistent with those expected from their numbers of amino acids. FCS measurement of monomer and tandem EGFPn in aqueous solution showed that their diffusion times also increased with molecular weight. Comparison of the measured diffusion time with the calculated diffusion time according to Perrin's equation (35,36) indicated that the tandemly linked EGFPn behaved like rod-like molecules. The fact

that diffusion times of tandem series of EGFP are proportional to their lengths in aqueous solution indicates that the proteins could be employed as molecular rulers (MR) in living cells.

Combining a well-defined MR with the high sensitivity of FCS measurement make possible analysis of protein mobility in living cells, in particular in the nucleus. In contrast to the cytoplasm, our results showed that there were two kinds of diffusional mobility in the nucleus, both of which also depended on the length of MR as shown in solution and cytoplasm. One was the fast-diffusion-mobility of tandem EGFP$_n$ found in the nucleoplasm as well as in the cytoplasm, in which the first component had a fraction above 90%, reflecting the free diffusion of the MR (represented by D of the first components in NP; Table 1). The other was the slow-diffusion-mobility (represented by D of the second components in NL; Table 1) observed in the nucleolus. The second component of the fast-diffusion-mobility in nucleoplasm showed a very slow diffusion (10^4–10^5 μs) with fractions under 10%, indicating no length dependency and no significant change by TSA treatment. The first component of the slow-diffusion-mobility (represented by D of the first components in NL, Table 1) in nucleolus was almost equivalent to the first component of the fast-diffusion-mobility in nucleoplasm (represented by D of the first components in NP, Table 1). There was no significant change in the diffusion time and the fraction for the first component of the fast-diffusion-mobility and for the second component of the slow-diffusion-mobility by TSA treatment (C. Pack and M. Kinjo, unpublished data). The result of FCS before and after TSA treatment was well consistent with LSM observation using two-color imaging (supplementary Figs. S1 and S5). Previous studies (4,38,43) using LSM observation of labeled dextran with various sizes showed that a globular protein with molecular weight of 1 MD (an apparent pore size of 14 nm) might be no limitation in access to chromatin. Because molecular weights of tandem EGFP$_n$ are much smaller than 1 MD, tandem EGFP$_n$ might freely access the two types of chromatin.

A study of FCS and monomer EGFP using both a two-component model and an anomalous subdiffusion model analysis (14) has shown that the diffusion of EGFP in the nucleus was much more complex than in the cytosol. The study described averaged diffusional mobility of EGFP in the entire nucleus but not in each compartments in the nucleus such as the nucleolus, and suggested that the ratio of diffusion mobilities in cells and in solution was not dependent on the two models used. The fast-diffusion-mobility of tandem GFP$_n$ in the cytoplasm and the nucleoplasm was dependent on length. The ratio of diffusion time in each compartment to that in solution showed that the apparent viscosities of the cytoplasm and nucleoplasm were identical. In addition, the apparent viscosity in the three cell lines (HeLa, COS7, and HEK293) was found to be ~3.5-fold higher than in aqueous solution. The viscosities in the cytoplasm and the nucleoplasm were well consistent with previous studies using FRAP (9,13) and using FCS (14).

We investigated the protein mobility in the nucleolar microenvironment of living cells in detail. The size and shape of the nucleolus during each phase of the cell cycle are not constant. Moreover, it was not easy to discriminate between the nucleoplasm and nucleolus in the cells weakly expressing the monomer and tandem EGFP$_n$. We marked the nucleolus with mRFP-tagged fibrillarin to distinguish it from the nucleoplasm. Our observations in the nucleolus (Fig. 5 E and Table 1) indicated that mobility of the inert EGFP and tandem EGFP$_n$ in the nucleolus was also dependent on the length of the protein, but that the mobility was ~17-fold slower for HeLa and 24-fold slower for COS7 than in aqueous solution. Nevertheless, assuming a random walk model, the result suggested that it would take the tandem proteins just a few seconds to travel a distance of 4 μm, roughly the diameter of a nucleolus. Rapid association or exchange of GFP-fibrillarin (0.046 μm^{2}s^{-1}) (12) and GFP-B23 (0.08 μm^{2}s^{-1}) (32) in the nucleolus was observed by FRAP. These results suggested that the nucleolus is not a static protein mass such as aggregates, and that proteins were dynamically exchanged between the nucleoplasm and the nucleolus. EGFP tagged fibrillarin was shown to have diffusion constants of 0.53 μm^{2}s^{-1} even in the nucleoplasm (12). On the other hand, diffusion of the MR in the nucleolus was much faster than for the nucleolar proteins (Table 1). For instance, the diffusion constants of tandem EGFP$_2$ were 14.9 ± 0.8 and 3.8 ± 0.5 μm^{2}s^{-1} in the nucleoplasm and the nucleolus of the HeLa cell, respectively, although the molecular weight and shape of EGFP$_2$ might be similar to EGFP-tagged fibrillarin (60 kD). Our observations indicated that the architecture of nucleolus was not very tight and some proteins, at least GFP$_n$, could be almost freely accessible inside of the compartment, because the mobility of GFP$_n$ was only slowed down about one-fifth compared with the nucleoplasm and the cytoplasm. Consequently, our study of MR mobility in the nucleoplasm and the nucleolus might be very helpful to understand the variability of mobility of microinjected labeled macromolecules in the nucleus (3,13) or the restricted mobility of monomeric EGFP (14) and various nuclear proteins (12,20, 32,41,49). In those studies, the complex microenvironment inside of the nucleolus was not considered in detail, even though the mobilities of the nuclear proteins were measured in the nucleolus and the interactions with nucleoli were analyzed.

Recent LSM observation of human U2OS cells expressing yellow fluorescent protein tagged H2B and electron microscopic observation of ATP-depleted cells have shown that the chromatin structure changes with nuclear shrinkage under energy depletion, and suggest that movement of mRNA-protein complexes (mRNPs) is constrained by the structural changes in the nucleus (20). It would be interesting to know whether the redistribution of the chromatin structure by energy depletion also affects other small proteins, and whether the nucleolar microenvironment is also changed by ATP depletion. To determine whether the diffusion of the longest

EGFP$_5$ in the nucleolar microenvironment was affected by the cellular metabolism, we treated HeLa cells expressing EGFP$_5$ with metabolic inhibitors 2-DG and NaN$_3$. Interestingly, our results showed that the diffusion of EGFP$_5$ in the nucleolus was slowed down by ATP depletion, but that in the cytoplasm and the nucleoplasm it was only slightly changed. The small change of EGFP$_5$ mobility (Fig. 6 B) in the nucleoplasm suggested that the microenvironment of nucleoplasm was not so changed. This result indicated that the mobility of proteins smaller than mRNP complex was not sensitive to the structural change in the nucleoplasm (20). Otherwise, the energy depletion would change large nuclear matrix structures (50–52), which affect the much larger molecular size of mRNP ($r \sim 133$ nm as a circular mRNP with 2.8 kb) rather than that of EGFP$_5$ (longitudinal length, ~ 28 nm). Recent reports have indicated that nuclear diffusion can be limited by a mesoscale viscosity for particles that are larger than 100 nm in diameter (53). In contrast, the change of EGFP$_5$ mobility in the nucleolus induced by ATP depletion suggested that the effect of energy depletion on the microenvironment of the nucleolus was bigger than that of the nucleoplasm and cytoplasm, even though the origin of the significant mobility change in the nucleolus was not clear. Nevertheless, our results clearly indicate that the microenvironment of the nucleolus is physiologically very different from that of the nucleoplasm. It is interesting to note that the two motor proteins, nuclear actin and myosin I are related to rDNA and are required for RNA polymerase I transcription (54). Such ATP-binding motor proteins can modify the nucleolar microenvironment.

In this study, we have demonstrated that combination of FCS and oligomeric EGFP$_n$ with different lengths is a novel method to elucidate the nuclear microenvironment of living cells. The microenvironment of the two compartments in the nucleus can now be differentiated and analyzed by using tandem MR, two-color imaging, and FCS. We found that MR EGFP$_n$, which is presumably inert, could rapidly diffuse inside of the cell nucleolus as well as the nucleoplasm depending only on the length of the protein. Our experimental system can be applied to understanding the mobility of other functional proteins in the nucleolus as well as in the cytoplasm and the nucleoplasm. More importantly, it is also suggested that the microenvironment of the nucleolus is very sensitive to pharmacological energy depletion compared to that of the cytoplasm and the nucleoplasm. Consequently, it is concluded that the physiological state of the nucleolar microenvironment can be understood through mobility analysis of tandem MR in living cells. Combining this method with other fluorescence microscopic methods such as time-lapse microscopy will allow complementary analysis of the nucleolar microenvironment of various cell types and single cells while varying the cell cycle or other physiological conditions such as cell stresses. Effects of GTP depletion or specific inhibitors such as actinomycin D, which primarily affects ribosome biogenesis in the nucleolus through the inhibition of RNA polymerase transcription, will also be important to understand the relations between the nucleolar microenvironment and physiological conditions in detail.

SUPPLEMENTARY MATERIAL

An online supplement to this article can be found by visiting BJ Online at http://www.biophysj.org.

REFERENCES

1. Misteli, T. 2001. Protein dynamics: implications for nuclear architecture and gene expression. *Science.* 291:843–847.

2. Pederson, T. 2000. Diffusional protein transport within the nucleus: a message in the medium. *Nat. Cell Biol.* 2:E73–E74.

3. Carmo-Fonseca, M., M. Platani, and J. R. Swedlow. 2002. Macromolecular mobility inside the cell nucleus. *Trends in Cell Biol.* 12: 491–5.

4. Görisch, S. M., P. Lichter, and K. Rippe. 2005. Mobility of multisubunit complexes in the nucleus: accessibility and dynamics of chromatin subcompartments. *Histochem. Cell Biol.* 123:217–228.

5. Houtsmuller, A. B., S. Rademakers, A. L. Nigg, D. Hoogstraten, J. H. J. Hoeijmakers, and W. Vermeulen. 1999. Action of DNA repair endonuclease ERCC1/XPF in living cells. *Science.* 284:958–961.

6. Phair, R. D., P. Scaffidi, C. Elbi, J. Vecerová, A. Dey, K. Ozato, D. T. Brown, G. Hager, M. Bustin, and T. Misteli. 2004. Global nature of dynamic protein-chromatin interactions in vivo: three-dimensional genome scanning and dynamic interaction networks of chromatin proteins. *Mol. Cell. Biol.* 24:6393–6402.

7. Verkman, A. S. 2002. Solute and macromolecule diffusion in cellular aqueous compartments. *Trends Biochem. Sci.* 27:27–33.

8. Brock, R., M. A. Hink, and T. M. Jovin. 1998. Fluorescence correlation microscopy of cells in the presence of autofluorescence. *Biophys. J.* 75: 2547–2557.

9. Kao, H. P., J. R. Abney, and A. S. Verkman. 1993. Determinants of the translational mobility of a small solute in cell cytoplasm. *J. Cell Biol.* 120:175–184.

10. Kues, T. R. Peters, and U. Kubitscheck 2001 Visualization and tracking of single protein molecules in the cell nucleus. *Biophys. J.* 80: 2954–67.

11. Luby-Phelps, K. P.E. Castle, D.L. Taylor, and F. Lanni 1987. Hindered diffusion of inert tracer particles in the cytoplasm of mouse 3T3 cells. *Proc. Natl. Acad. Sci. USA.* 84: 4910–3.

12. Phair, R. D., and T. Misteli. 2000. High mobility of proteins in the mammalian cell nucleus. *Nature.* 404:604–609.

13. Seksek, O., J. Biwersi, and A. S. Verkman. 1997. Translational diffusion of macromolecule-sized solutes in cytoplasm and nucleus. *J. Cell Biol.* 138:131–142.

14. Wachsmuth, M., W. Waldeck, and J. Langowski. 2000. Anomalous diffusion of fluorescent probes inside living cell nuclei investigated by spatially resolved fluorescence correlation spectroscopy. *J. Mol. Biol.* 298:677–689.

15. Weiss, M. M. Elsner, F. Kartberg, and T. Nilsson. 2004. Anomalous subdiffusion is a measure for cytoplasmic crowding in living cells. *Biophys. J.* 87: 3518–24.

16. Lukacs, G. L., P. Haggie, O. Seksek, D. Lechardeur, N. Freedman, and A. S. Verkman. 2000. Size-dependent DNA mobility in cytoplasm and nucleus. *J. Biol. Chem.* 275:1625–1629.

17. Sprague, B. L., R. L. Pego, D. A. Stavreva, and J. G. McNally. 2004. Analysis of binding reactions by fluorescence recovery after photobleaching. *Biophys. J.* 86:3473–3495.

18. Schmiedeberg, L., K. Weisshart, S. Diekmann, G. M. Hoerste, and P. Hemmerich. 2004. High- and low-mobility populations of HP1 in heterochromatin of mammalian cells. *Mol. Biol. Cell.* 15:2819–2833.

19. McNally, J. G., W. G. Müller, D. Walker, R. Wolford, and G. L. Hager. 2000. The glucocorticoid receptor: rapid exchange with regulatory sites in living cells. *Science.* 287:1262–1265.

20. Shav-Tal, Y., X. Darzacq, S. M. Shenoy, D. Fusco, S. M. Janicki, D. L. Spector, and R. H. Singer. 2004. Dynamics of single mRNPs in nuclei of living cells. *Science.* 304:1797–1800.

21. Kinjo, M., and R. Rigler. 1995. Ultrasensitive hybridization analysis using fluorescence correlation spectroscopy. *Nucleic Acids Res.* 23: 1795–1799.

22. Nomura, Y., H. Tanaka, L. Poellinger, F. Higashino, and M. Kinjo. 2001. Monitoring of in vitro and in vivo translation of green fluorescent protein and its fusion proteins by fluorescence correlation spectroscopy. *Cytometry.* 44:1–6.

23. Pack, C., K. Aoki, H. Taguchi, M. Yoshida, M. Kinjo, and M. Tamura. 2000. Effect of electrostatic interactions on the binding of charged substrate to GroEL studied by highly sensitive fluorescence correlation spectroscopy. *Biochem. Biophys. Res. Commun.* 267:300–304.

24. Saito, K., E. Ito, Y. Takakuwa, M. Tamura, and M. Kinjo. 2003. In situ observation of mobility and anchoring of PKCβI in plasma membrane. *FEBS Lett.* 541:126–131.

25. Terada, S., M. Kinjo, and N. Hirokawa. 2000 Oligomeric tubulin in large transporting complex is transported via kinesin in squid giant axons. *Cell.* 103:141–55.

26. Yoshida, N., M. Kinjo, and M. Tamura. 2001. Microenvironment of endosomal aqueous phase investigated by the mobility of micropartcles using fluorescence correlation spectroscopy. *Biochem. Biophys. Res. Commun.* 280:312–318.

27. Ormö, M., A. B. Cubitt, K. Kallio, L. A. Gross, R. Y. Tsien, and S. J. Remington. 1996. Crystal structure of the Aequorea Victoria green fluorescent protein. *Science* 273:1392–5.

28. Tsien, R. Y. 1998. The green fluorescent protein. *Annu. Rev. Biochem.* 57:509–544.

29. Yang, F., L. G. Moss, and G. N. Phillips. 1996. The molecular structure of green fluorescent protein. *Nat. Biotechnol.* 14:1246–1251.

30. Kimura, H., and P. R. Cook. 2001. Kinetics of core histones in living human cells: little exchange of H3 and H4 and some rapid exchange of H2B. *J. Cell Biol.* 153:1341–1353.

31. Kanda, T., K. F. Sullivan, and G. M. Wahl. 1998. Histone-GFP fusion protein enables sensitive analysis of chromosome dynamics in living mammalian cells. *Curr. Biol.* 8:377–385.

32. Chen, D., and S. Huang. 2001. Nucleolar components involved in ribosome biogenesis cycle between the nucleolus and nucleoplasm in interphase cells. *J. Cell Biol.* 153:169–176.

33. Saito, K., M. Tamura, and M. Kinjo. 2004. Direct detection of caspase-3 activation in single live cells by cross-correlation analysis. *Biochem. Biophys. Res. Commun.* 324:849–854.

34. Weisshart, K., V. Jungel, and S. J. Briddon. 2004. The LSM 510 META-ConfoCor 2 system: an integrated imaging and spectroscopic platform for single-molecule detection. *Cur. Pharm. Biotech.* 5: 135–154.

35. Cantor, C. R., and P. R. Schimmel. 1980. *In* Biophysical Chemistry Part II: Chapter 10. Techniques for the Study of Biological Structure and Function. W. H. Freeman, New York. 560–567.

36. Björling, S., M. Kinjo, Z. Földes-Papp, E. Hagman, P. Thyberg, and R. Rigler. 1998. Fluorescence correlation spectroscopy of enzymatic DNA polymerization. *Biochemistry.* 37:12971–12978.

37. Rigler, R., Ü. Mets, J. Widengren, and P. Kask. 1993. Fluorescence correlation spectroscopy with high count rate and low background: analysis of translational diffusion. *Eur. Biophys. J.* 22:169–175.

38. Görisch, S. M., K. Richter, M. O. Scheuermann, H. Herrmann, and P. Lichter. 2003. Diffusion-limited compartmentalization of mammalian cell nuclei assessed by microinjected macromolecules. *Exp. Cell Res.* 289:282–294.

39. Swaminathan, R., C. P. Hoang, and A. S. Verkman. 1997. Photobleaching recovery and anisotropy decay of green fluorescent protein EGFP-S65T in solution and cells: cytoplasmic viscosity probed by green fluorescent protein translational and rotational diffusion. *Biophys. J.* 72:1900–1907.

40. Terry, B. R., E. K. Matthews, and J. Haseloff. 1995. Molecular characterization of recombinant green fluorescent protein by fluorescence correlation microscopy. *Biochem. Biophys. Res. Commun.* 217: 21–7.

41. Wachsmuth M., T. Weidemann, G. Müller, U. W. Hoffmann-Rohrer, T. A. Knoch, W. Waldeck, and J. Langowski. 2003. Analyzing intracellular binding and diffusion with continuous fluorescence photobleaching. *Biophys. J.* 84:3353–3363.

42. Larson, D. R., Y. M. Ma, V. M. Vogt, and W. W. Webb. 2003. Direct measurement of Gag-Gag interaction during retrovirus assembly with FRET and fluorescence correlation spectroscopy. *J. Cell Biol.* 162: 1233–1244.

43. Görisch, S. M., M. Wachsmuth, K. Fejes Tóth, P. Lichter, and K. Rippe. 2005. Histone acetylation increases chromatin accessibility. *J. Cell Sci.* 118:5825–5834.

44. Leung, A. K., D. Gerlich, G. Miller, C. Lyon, Y. W. Lam, D. Lleres, N. Daigle, J. Zomerdijk, J. Ellenberg, and A. I. Lamond. 2004. Quantitative kinetic analysis of nucleolar breakdown and reassembly during mitosis in live human cells. *J. Cell Biol.* 166:787–800.

45. Olson, M. O. J., and M. Dundr. 2005. The moving parts of the nucleolus. *Histochem. Cell Biol.* 123:203–216.

46. Olson, M. O. J., M. Dundr, and A. Szebeni. 2000. The nucleolus: an old factory with unexpected capabilities. *Trends Cell Biol.* 10:189–196.

47. Peters, R. 1983. Nuclear envelope permeability measured by fluorescence microphotolysis of single liver cell nuclei. *J. Biol. Chem.* 258: 11427–11429.

48. Davis, L. I. 1995. The nuclear pore complex. *Annu. Rev. Biochem.* 64:865–896.

49. Weidemann T., M. Wachsmuth, T. A. Knoch, G. Müller, W. Waldeck, and J. Langowski 2003. Counting nucleosomes in living cells with a combination of fluorescence correlation spectroscopy and confocal imaging. *J. Mol. Biol.* 334:229–40.

50. Nickerson, J. A. 2001. Experimental observations of a nuclear matrix. *J. Cell Sci.* 114:463–474.

51. Rando, O. J., K. Zhao, and G. R. Crabtree. 2000. Searching for a function for nuclear actin. *Trends Cell Biol.* 10:92–97.

52. Pederson, T., and U. Aebi. 2003. Actin in the nucleus: what form and what for? *J. Struct. Biol.* 140:3–9.

53. Tseng, Y., J. S. Lee, T. P. Kole, I. Jiang, and D. Wirtz. 2004. Microorganization and visco-elasticity of the interphase nucleus revealed by particle nanotracking. *J. Cell Sci.* 117:2159–2167.

54. Philimonenko, V. V., J. Zhao, S. Iben, H. Dingova, K. Kysela, M. Kahle, H. Zentgraf, W. A. Hofmann, P. Lanerolle, P. Hozak, and I. Grummt. 2004. Nuclear actin and myosin I are required for RNA polymerase I transcription. *Nat. Cell Biol.* 6:1165–1172.

Lateral Mobility of Membrane-Binding Proteins in Living Cells Measured by Total Internal Reflection Fluorescence Correlation Spectroscopy

Yu Ohsugi,* Kenta Saito,[†] Mamoru Tamura,* and Masataka Kinjo*

Laboratory of *Supramolecular Biophysics and [†]Nanosystems Physiology, Research Institute for Electronic Science, Hokkaido University, Sapporo, Japan

ABSTRACT   Total internal reflection fluorescence correlation spectroscopy (TIR-FCS) allows us to measure diffusion constants and the number of fluorescent molecules in a small area of an evanescent field generated on the objective of a microscope. The application of TIR-FCS makes possible the characterization of reversible association and dissociation rates between fluorescent ligands and their receptors in supported phospholipid bilayers. Here, for the first time, we extend TIR-FCS to a cellular application for measuring the lateral diffusion of a membrane-binding fluorescent protein, farnesylated EGFP, on the plasma membranes of cultured HeLa and COS7 cells. We detected two kinds of diffusional motion—fast three-dimensional diffusion (D_1) and much slower two-dimensional diffusion (D_2), simultaneously. Conventional FCS and single-molecule tracking confirmed that D_1 was free diffusion of farnesylated EGFP close to the plasma membrane in cytosol and D_2 was lateral diffusion in the plasma membrane. These results suggest that TIR-FCS is a powerful technique to monitor movement of membrane-localized molecules and membrane dynamics in living cells.

INTRODUCTION

Fluorescence correlation spectroscopy (FCS) monitors the fluctuations in fluorescence intensity caused by fluorophores diffusing freely in a small observation volume. The measured fluctuation signals are converted to diffusion constants and the absolute number of fluorescently labeled particles at the single-molecule level (1). FCS has been used as a powerful tool for characterizing the dynamic behavior and kinetic properties of biochemical reactions in vitro (2–6) and in vivo (7–13).

Intracellular signaling pathways are triggered by the binding of a ligand to its receptor, stimulation, stress, etc., on the cell surface to regulate cell activities (proliferation, differentiation, apoptosis, etc.). Hence, elucidation of the molecular interactions on the plasma membrane is required for understanding of cellular functions and is expected to be useful for the discovery of drug targets as well. Growing numbers of FCS studies at the single-molecule level have revealed the kinetic properties of biomolecular interactions in subcellular organelles in living cells (7–12). However, with confocal optics-based FCS, there are some difficulties in measuring molecular diffusion on the plasma membrane because of the relatively low spatial resolution along the optical axis and the very large scattering of background light at the coverslip. To improve this, we combined FCS with objective-lens type total internal reflection fluorescence microscopy (TIR-FM). For excitation light, objective-lens type TIR-FM generates an evanescent field, using a totally internally reflected laser beam after it passes through the objective (14). The depth of the evanescent field is very thin

(100~200 nm). Therefore, the field excites only fluorophores near the surface. The narrow excitation achieved by the evanescent field allows visualization of molecular dynamics at the plasma membrane without interference from fluctuations in cytosol (15). FCS combined with TIR-FM, i.e., TIR-FCS (16), has developed into a useful method to quantitatively study ligand-receptor associations and kinetics on a supported membrane (17,18). However, there has been no report on the application of TIR-FCS to cell biology.

Herein, for the first time, we report cellular application of TIR-FCS for measuring lateral diffusion of membrane-binding proteins, carried out as a feasibility study for the development of TIR-FCS. The TIR-FCS setup is constructed with an FCS detector unit and objective-type TIR-FM (Fig. 1) (19,20). By using TIR-FCS, we observed lateral diffusion of membrane binding proteins, i.e., the enhanced green fluorescent protein (EGFP)-fused farnesylated domain (EGFP-F) in the plasma membrane facing the coverslip in HeLa cells and COS7 cells. Conventional FCS and single-molecule tracking (SMT) using a charge-coupled device camera were carried out to assess the obtained TIR-FCS data.

MATERIALS AND METHODS

Sample preparation

EGFPs were prepared using a wheat-germ extract (cell-free) translation system (21). Glass chambers (384-well glass-bottom plate, Olympus, Tokyo, Japan) for in vitro TIR-FCS experiments were treated with a blocking reagent (N101, NOF, Tokyo, Japan) to prevent nonspecific adsorption of EGFPs.

Cells were cultured in a 5% CO_2 humidified atmosphere at 37°C in Dulbecco's modified Eagle's medium (DMEM) supplemented with 10% fetal bovine serum, 2 × 10^5 U/L penicillin G, and 200 mg/L streptomycin sulfate. For microscopy the cells were grown on glass-base dishes (ϕ12 mm, Asahi Technoglass, Chiba, Japan).
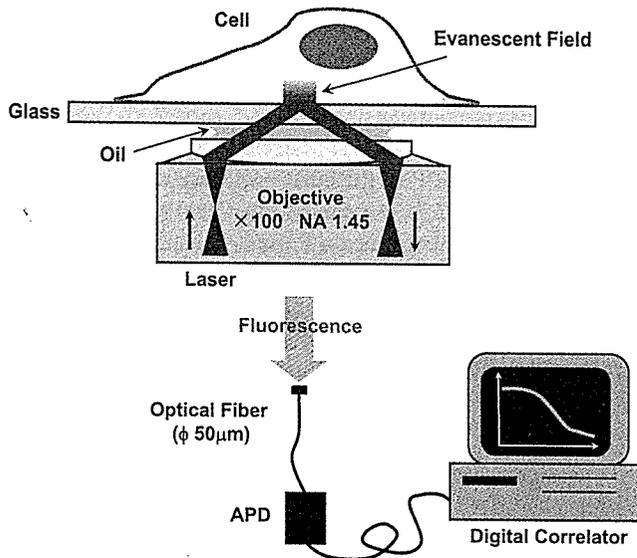
FIGURE 1 Schematic diagram of objective-type TIR-FCS setup for cellular application. Total internal reflection (TIR) illumination, achieved by objective-lens type TIR-FM, produces an evanescent field. Cultured cells are illuminated by the evanescent field near the glass surface. Fluorescence signals are focused into an optical fiber (ϕ50 μm) and collected by an Avalanche photodiode (APD). The fluorescence autocorrelation function is calculated by a digital correlator.

Octadecyl rhodamine B chloride (R18) was purchased from Molecular Probes (Eugene, OR). For R18 labeling, COS7 cells were incubated with 2 ml of DMEM and 100 μl of R18 (1 μM) on poly-L-lysine-coated glass-base dishes 5 h before TIR-FCS measurement. Before the experiments, COS7 cells were washed five times with PBS.

Cells were transfected with 1.0 μg of plasmid DNA of pEGFP-C1 or pEGFP-F (Clontech, Palo Alto, CA) (note that although these products are now commercially unavailable, the vector information is provided as a courtesy on the company's website, http://www.clontech.com/clontech/) and 3.0 μl of FuGENE6 (Roche Molecular Biochemicals, Mannheim, Germany) per glass-base dish 15 h before TIR-FCS measurement or single-molecule imaging. During microscopic observation, cells were maintained in phenol red-free DMEM/F-12 (Invitrogen, Carlsbad, CA) at room temperature.

TIR-FCS setup and measurement

The TIR-FCS setup was constructed with an inverted microscope (TE2000, Nikon, Kanagawa, Japan), observation unit for TIR illumination (Nikon), a multimode fiber with a ϕ50 μm-diameter core, an avalanche photodiode (SPCM-AQ-141-FC, EG&G, Vaudreuil, Quebec, Canada), and a digital correlator (ALV 5000/E, ALV, Langen, Germany). The objective-type TIR-FM was equipped with a ×100 oil-immersion objective (Plan Apo, NA = 1.45, Nikon). The samples were excited at the 488-nm laser line of a semiconductor laser (488-20CDRH, Coherent, CA), and fluorescence signals were detected through a dichroic mirror (>505 nm) and a bandpass filter (510–560 nm) for EGFP and a longpass filter (>520 nm) for R18.

Determination of TIR-FCS observation volume

Fluorescence autocorrelation functions (FAFs), $G(\tau)$, were acquired online with a digital correlator and fitted by a one-component model (17,19,20) for the control experiments on fluorescein in 10 mM Tris buffer (pH 8.0) to determine the structure parameter defined by $\omega = h/\omega_{xy}$ (20). The values h and ω_{xy} are the height and radius of the TIR-FCS detection volume, respectively.

$$G(\tau) = \frac{\langle I(t) \cdot I(t+\tau) \rangle}{\langle I(t) \rangle^2}$$

$$= 1 + \frac{\gamma}{N}\left[1 + \frac{p}{1-p}\exp\left(-\frac{\tau}{\tau_t}\right)\right]\left(1 + \frac{\omega^2\tau}{\tau_z}\right)^{-1}$$

$$\times \left\{\left(1 - \frac{\tau}{2\tau_z}\right)w\left(i\sqrt{\frac{\tau}{4\tau_z}}\right) + \sqrt{\frac{\tau}{\pi\tau_z}}\right\}, \qquad (1)$$

where the value N is the average number of fluorescent particles in an effective volume. The value γ is a correction factor, describing the deviation of the effective volume. Here, we used the value $\gamma = 1/3.4$ according to previous research (20). The value p is the average fraction of molecules that are in the triplet state in the effective volume. The value τ_t is the triplet state decay time. The axial diffusion time is given by $\tau_z = h^2/4D$. The value D denotes the diffusion constant and w is the complex generalization of the error function, $w(x) \equiv \exp(-x^2)\,\mathrm{erfc}(-ix)$.

To estimate the size of the observation volume, we determined the value of h from the relation $h = (4D\tau_z)^{1/2}$, using the diffusion constant of fluorescein ($D = 3.0 \times 10^{-6}$ cm^2/s (20)) and the average value of τ_z obtained by fitting. In the case of cellular measurements, we used the same values of ω, h, and ω_{xy} as for in vitro experiments.

Analysis of TIR-FCS data

Fitting analyses of FAFs were carried out to yield the diffusion constants, where the value of ω was fixed, based on 10 measurements from control experiments on fluorescein. For R18-labeled COS7 cells, a model of two-dimensional diffusion (Eq. 2) was employed to fit the data (22),

$$G(\tau) = 1 + \frac{\gamma}{N}\left[\sum_i F_i\left(1 + \frac{\tau}{\tau_{i,xy}}\right)^{-1}\right], \qquad (2)$$

where F_i is the fraction of fluorophores laterally diffusing on the surface. The lateral diffusion time for two-dimensionally diffusing fluorophores on the plasma membrane is given by $\tau_{i,xy} \equiv \omega_{xy}^2/4D_i$ ($i = 1, 2$).

The fitting model for experiments of EGFP-F expressed in cells, in which fluorescence fluctuations resulting from both faster free diffusion through the evanescent field and slower lateral diffusion parallel to the surface, was applied to a two-component model containing the terms of the two-dimensional model:

$$G(\tau) = 1 + \frac{\gamma}{N}\left[F_1\left(1 + \frac{\omega^2\tau}{\tau_{1,z}}\right)^{-1}\left\{\left(1 - \frac{\tau}{2\tau_{1,z}}\right)w\left(i\sqrt{\frac{\tau}{4\tau_{1,z}}}\right)\right.\right.$$

$$\left.\left. + \sqrt{\frac{\tau}{\pi\tau_{1,z}}}\right\} + F_2\left(1 + \frac{\tau}{\tau_{2,xy}}\right)^{-1}\right]. \qquad (3)$$

The value $\tau_{1,z}$ is the axial diffusion time of three-dimensionally diffusing fluorophores near the plasma membrane in cytosol. In fact, we used a model function containing a term accounting for triplet state kinetics as described in previous works (19,20).

Confocal FCS and single-molecule tracking

Confocal FCS measurements were carried out with a ConfoCor 2 (Carl Zeiss, Jena, Germany) (11). Single-molecule tracking was performed using a TIR fluorescence microscope equipped with a cooled charge-coupled device camera (Cascade 650, Photometrics, Tucson, AZ) and an image intensifier (C8600-03, Hamamatsu Photonics, Hamamatsu, Japan). The single fluorescent molecules were tracked for 0.67 $\sim$ 2 s (20$\sim$60 frames) using imaging software (Meta Morph, Universal Imaging, Downingtown, PA). The single-molecule trajectories were analyzed with mean-square displacement

(MSD) given by $\langle r^2 \rangle = 4D\tau$. The two-dimensional MSD, $\langle r^2 \rangle$, was calculated for each particle, where r denotes the displacement of the fluorescent particle during each time interval, τ indicates multiples of 33.3 ms, and $\langle \ldots \rangle$ denotes the average over the tracking duration (23,24).

RESULTS

TIR-FCS in vitro experiments

We first carried out TIR-FCS measurements of fluorescein in Tris-buffered solution (10 mM, pH 8.0), in control experiments to determine the TIR-FCS observation volume. Fluorescence fluctuation of fluorescein diffusing near the glass surface in aqueous solution was detected by TIR-FCS (Fig. 2 a). The best fitting of the autocorrelation functions by Eq. 1 yielded the average value of structure parameter $\omega = $
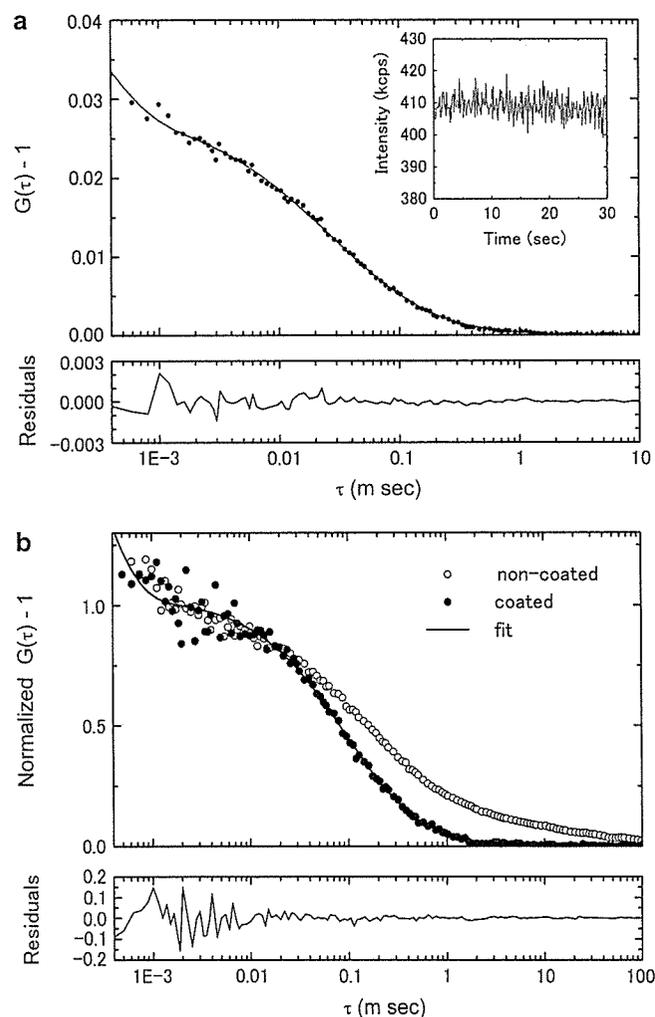
FIGURE 2 Autocorrelation function of TIR-FCS control experiments. Control measurements were carried out on samples. (a) 300 nM fluorescein in 10 mM Tris (pH 8.0). Fitting analysis with Eq. 1 yielded $N = 10.4$, $p = 44\%$, $\tau_t = 0.3$ μs, $\tau_z = 2.7$ μs, and $\omega = 0.15$. (b) EGFP in 10 mM Tris (pH 8.0) near the glass surface with ($\bullet$) and without ($\bigcirc$) blocking treatment. The best fit of the data ($\bullet$) to Eq. 1 gave $N = 0.6$, $\tau_t = 0.2$ μs, $p = 78\%$, and $\tau_z = 16$ μs. The structure parameter ω was fixed to 0.16.

0.16 and axial diffusion time $\tau_z = 3.1$ μs. Therefore, h was estimated to be 61 nm and $\omega_{xy} = 381$ nm.

As the next step, EGFP diffusing near the glass surface in Tris buffer was measured using TIR-FCS (Fig. 2 b). With the blocking reagent treatment (see Materials and Methods) only free diffusion of EGFP in the buffer solution was measured by TIR-FCS (Fig. 2 b, solid circles). On the other hand, when the glass chamber was not treated, nonspecific binding of EGFPs to the glass surface gave a long-time component of autocorrelation (Fig. 2 b, open circles). The overall background signal for the negative control with the blocking reagent was ~4.0 kcps (10^3 counts/second). The blocking reagent exhibited weak fluorescence but gave no autocorrelation function. The fitting analyses with Eq. 1, where $\omega = 0.16$ was fixed, yielded diffusion constants of EGFP in Tris buffer ($D = 6.9 \times 10^{-7}$ cm^2/s, Table 1). This value agreed well with the predicted value calculated from the cube root of fluorescein and the EGFP molecular weight ratio, according to the Stokes-Einstein equation, and was almost the same as that obtained using conventional FCS (7.8 $\times$ 10^{-7} cm^2/s, (25)). Fig. 2 b shows that the average signal $\langle S \rangle$ was 10.2 kcps, and the average background intensity $\langle B \rangle$ was 3.8 kcps. Fitting gave the number of fluorophores $N = 0.6$. The background-corrected values (26) of N and cpm were 0.2 and 27.8 kcps, respectively. Therefore, these results demonstrated that the TIR-FCS system was successfully set up.

TIR-FCS of EGFP in cytosol of HeLa cells

We also tried to measure EGFP diffusion in cytosol of HeLa cells using TIR-FCS. First, we carried out experiments with the same incident angle of the laser beam near θ_{max} ($\approx 72°$) as in the control experiments above, which resulted in a small evanescent field. However, no clear correlation curve was obtained (data not shown).

To gain stronger fluorescent signals, HeLa cells were illuminated with a deeper evanescent field ($\theta < 70°$), then correlation curves were observed (Fig. 3). Because of fast photobleaching, we could collect fluorescent signals from HeLa cells for only 10 s. Therefore, the ratio of signal/noise (S/N) was lower than for in vitro experiments. The background autofluorescence level of HeLa cells was ~5.0 kcps. With the same incident-angle of the laser, fluorescein

TABLE 1 TIR-FCS of EGFP in solution and living cells

EGFP	ω	D (cm^2/s)	n
In Tris buffer	0.16	6.9 $\pm$ 0.9 $\times$ 10^{-7}	10
	0.18	7.2 $\pm$ 0.7 $\times$ 10^{-7}	10
In HeLa cells	0.16	ND	
	0.18	2.7 $\pm$ 1.0 $\times$ 10^{-7}	23

Average diffusion constants (D) of EGFP in Tris buffer (pH 8.0) and HeLa cells measured using TIR-FCS. Structure parameter ω was fixed, based on the fitting results of fluorescein measurements. The value n is the number of measurements. ND, not determined. Means $\pm$ SD.
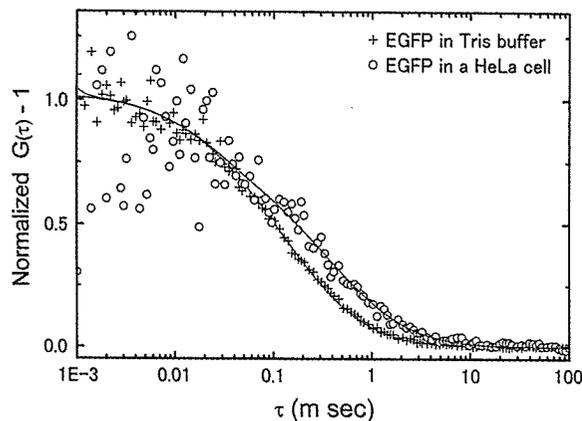
FIGURE 3 Autocorrelation functions of EGFP in aqueous solution and in cytosol of HeLa cells using TIR-FCS. Representative normalized autocorrelation functions of EGFP in Tris buffer solution (pH 8.0) (*red cross*) and in cytosol of HeLa cells (*blue circle*). Diffusion constants were given as 8.2×10^{-7} cm²/s in solution and 1.6×10^{-7} cm²/s in a HeLa cell by fitting.

in Tris-buffer solution was measured, and the fitting of the data gave $\omega = 0.18$. EGFP in solution was also measured in the same way (Fig. 3). By fitting of the FAFs with Eq. 1, where ω was fixed at 0.18, the average diffusion constants of EGFP were calculated to be $7.2 \pm 1.0 \times 10^{-7}$ cm²/s in solution and $2.7 \pm 1.0 \times 10^{-7}$ cm²/s in HeLa cells (Table 1). The values agreed well with previous research using confocal FCS measurement (solution: 7.8×10^{-7} cm²/s, HeLa: 2.4×10^{-7} cm²/s (25)). In comparison between the EGFP diffusion constants in aqueous solution and HeLa cells, the ratio (~2.7) reflects the difference of viscosity in Tris-buffer solution and cytosol of living cells (Table 1). These results showed the feasibility of using TIR-FCS to measure diffusion constants of molecules in living cells.

TIR-FCS of fluorescent lipophilic probes in cell membranes

To apply TIR-FCS to membrane-localized molecules in living cells, the fluorescent lipophilic probe, R18, which binds to the membrane, was observed by TIR-FCS in the plasma membrane of COS7 cells. The autocorrelation function for R18 in COS7 cellular membranes is shown in Fig. 4 (*black line*). The data were fitted well by a two-component model of two-dimensional diffusion (*blue line*), but not by a one-component model (*red line*). The fitting results yielded faster diffusion constants $5.7 \pm 8.6 \times 10^{-7}$ cm²/s ($40 \pm 16\%$) and slower diffusion constants $6.2 \pm 3.7 \times 10^{-9}$ cm²/s ($60 \pm 16\%$). Confocal FCS measurements were also carried out to confirm that there was not only one normal diffusive (lateral) motion but also a faster component of R18 on the cell membrane (Supplementary Material, Fig. S1). These results demonstrated that TIR-FCS was applicable for monitoring lateral diffusion of molecules on the cell membrane.
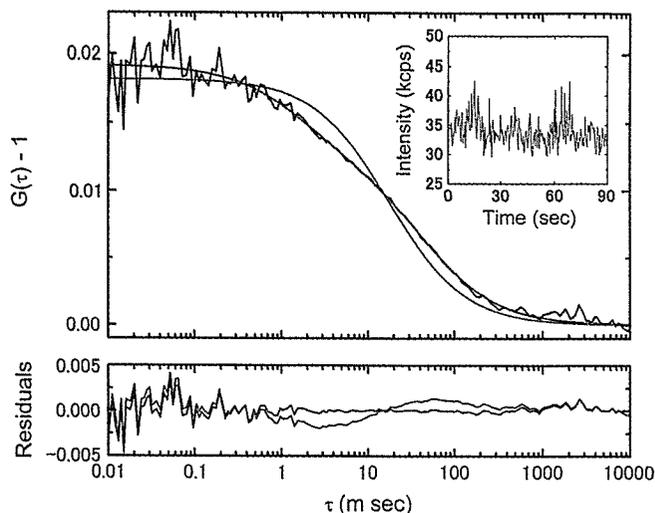

FIGURE 4 Autocorrelation function of R18 in cell membranes of living COS7 cells using TIR-FCS. Autocorrelation function of R18 in the cell membrane (*black line*) and fitting curves of one-component model (*red line*, Eq. 2, $i = 1$) and two-component model (*blue line*, Eq. 2, $i = 2$). The fit residues are shown in the bottom panel.

TIR-FCS of membrane binding protein in living cells

TIR-FCS was employed for observation of lateral diffusion of membrane-binding farnesylated EGFP (EGFP-F) in living cells. At its C-terminal 20-amino-acid region, EGFP-F contains a membrane-anchor domain from H-Ras (Fig. 5 *a*) (27,28). After modification of the domain by farnesylation and palmitoylation, the EGFP-F was located in the inner leaflet of the plasma membrane. Fig. 5 *b* shows that most EGFP-F was anchored in the plasma membrane; however, weak signals from cytosol were presumed to represent EGFP-F without fatty acid modification for membrane-anchorage.

To reduce background signals from cytosol and photobleaching, an evanescent field as thin as possible was formed by adjusting the incident angle of the excitation laser beam to $72°$, close to the maximum angle allowed by the numerical aperture of the objective (NA $= 1.45$), for total internal reflection. By such fine-tuning we could collect fluorescence signals from small areas of plasma membranes of HeLa cells transiently expressing EGFP-F (Fig. 5 *c*). When the cells were initially illuminated by the evanescent field for 90 s, the fluorescence intensity at the plasma membrane decreased to ~70% because of photobleaching. Thus, after the photobleaching we observed the fluorescence fluctuation using TIR-FCS. The obtained FAFs fit very well with the 3D2D two-component model (Eq. 3), using the fixed value of $\omega = 0.16$ (Fig. 5 *d*). We detected two kinds of diffusional motion: fast diffusion ($D_1 = 1.1 \pm 0.3 \times 10^{-7}$ cm²/s, $F_1 = 72\%$) derived from the three-dimensional term of the fitting model, and much slower diffusion ($D_2 = 5.6 \pm 2.2 \times 10^{-9}$ cm²/s, $F_2 = 28\%$) from the two-dimensional term (Fig. 5 *e*). D_1 was presumed to express freely-diffusing EGFP-F near the
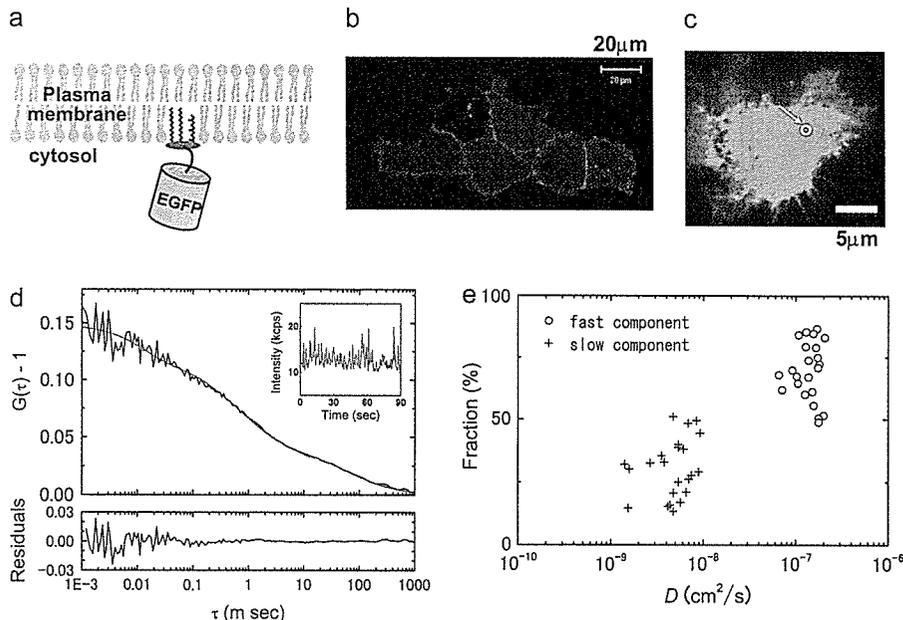
FIGURE 5 TIR-FCS measurements of HeLa cells expressing EGFP-F. (a) Schematic diagram of EGFP-F. EGFP-F are anchored in the inner surface of the plasma membrane by one farnesylation and two palmitoylations at its C-terminal region. (b) LSM image of HeLa cells expressing EGFP-F. Bar represents 20 μm. (c) TIR-FM image of an HeLa cell expressing EGFP-F. Arrow and small circle indicate TIR-FCS observation area. Bar represents 5 μm. (d) The black line shows the autocorrelation function acquired by TIR-FCS of EGFP-F and the red line shows the fitting curve. (Inset) Time course of the fluorescence intensities. The bottom panel shows the fit residue. (e) Distribution analysis of diffusion constants. Dispersion plots of diffusion constants and their fractions from TIR-FCS of EGFP-F.

plasma membrane in cytosol. Then confocal FCS was carried out to detect EGFP-F randomly moving in cytosol (three-dimensional model) and to measure its diffusion constant ($D_1 = 2.7 \pm 1.0 \times 10^{-7}$ cm^2/s, $F_1 = 59\%$, Table 2).

Single-molecule tracking of EGFP-F

We employed single-molecule tracking analysis to measure the diffusion constants of membrane-anchor EGFP-F. EGFP-F fluorescent signals were visualized as small spots (Fig. 6 a). The EGFP-F spots exhibited single-step photobleaching (Fig. 6 b), and the distribution of the fluorescence intensity of individual spots showed a Gaussian-like shape (data not shown). These aspects showed that visualization with single-molecule sensitivity was achieved. Some spots had almost double the intensity of single EGFP-F molecules because of the tendency for EGFP to dimerize. Lateral movements of single fluorescent particles were traced and the obtained trajectories are shown in Fig. 5 c. The mean-square displacement (MSD), $\langle r^2 \rangle$, was plotted against the time lag to calculate the diffusion constants of EGFP-F spots. The average diffusion constant was obtained as $4.7 \pm 4.6 \times 10^{-9}$ cm^2/s (Fig. 6 d).

TIR-FCS with a series of laser power

Generally, FCS may not be appropriate for monitoring slow diffusional motion such as lateral diffusion of membrane-binding molecules because of the high possibility of photobleaching artifacts. The problem is that photobleaching may result in a faster apparent diffusion time than the real one. When fluorescent molecules diffuse slowly they are likely to be bleached in the detection volume before they pass through it. Therefore, it is necessary to demonstrate that diffusion constants obtained by TIR-FCS really represent diffusional mobility rather than photobleaching dynamics. By using TIR-FCS, we observed EGFP-F in COS7 cells with a series of excitation laser power densities: 1.0, 0.5, and 0.25 μW/μm^2 (Fig. 7, a–c). These laser power densities were measured through the objective ($\theta = 0°$, epi-illumination). The laser power at the maximum was 1.0 μW/μm^2 in our TIR-FCS system. We were not able to obtain a clear autocorrelation function below 0.25 μW/μm^2. Each autocorrelation function was fitted with Eq. 3 as well as Fig. 5. There were differences in the fluorescence intensities (inset) and S/N ratios of the autocorrelation curves among the data for the three different laser powers. On the other hand, the diffusion constants of slow components (D_2) were almost the same (Table 3). We

TABLE 2 Comparison of TIR-FCS with other methods

| Method | Fast | | Slow | | |
	D_1 (cm^2/s)	F_1 (%)	D_2 (cm^2/s)	F_2 (%)	n
TIR-FCS	$1.1 \pm 0.3 \times 10^{-7}$	72 ± 11	$5.6 \pm 2.2 \times 10^{-9}$	28 ± 11	23
SMT	ND		$4.7 \pm 4.6 \times 10^{-9}$	100	127
Confocal FCS	$2.7 \pm 1.0 \times 10^{-7}$	59 ± 14	$7.0 \pm 8.6 \times 10^{-9}$	41 ± 14	42

Average diffusion constants (D), fraction (F) of EGFP-F expressed in HeLa cells measured using TIR-FCS, single-molecule tracking (SMT) and confocal FCS. The value n is the number of measurements (FCS) or EGFP-F molecules (SMT). ND, not determined. Means $\pm$ SD.
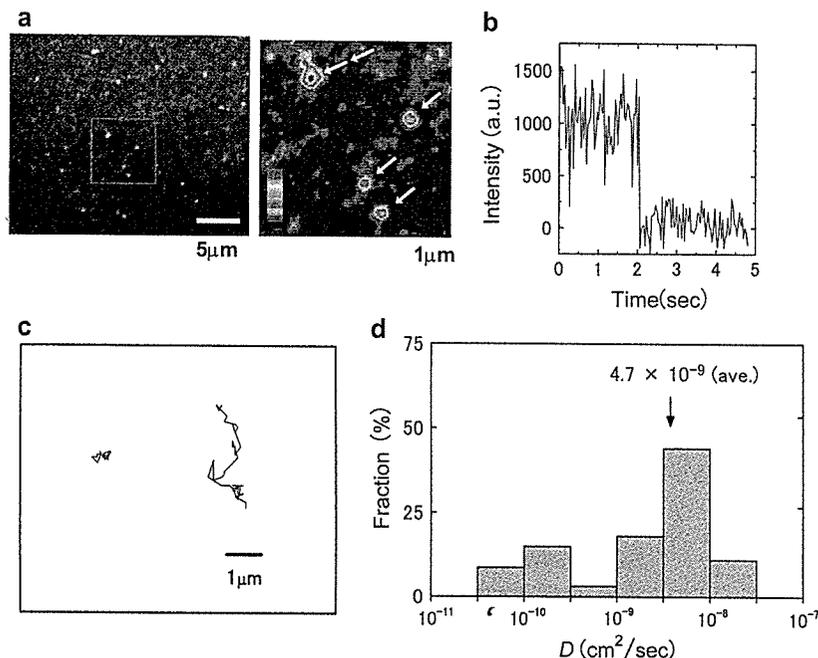
FIGURE 6 Single-molecule tracking of EGFP-F on plasma membrane. (*a*) Single fluorescent molecule images of EGFP-F expressed in HeLa cells. Bar represents 5 μm (*left*). Enlarged image of area surrounded by red rectangle. The fluorescence intensity is viewed in pseudocolor. Single molecules (*single arrowheads*) and a dimer (*double arrowheads*) of EGFP-F are shown. Bar represents 1 μm (*right*). (*b*) Time course of fluorescent intensity of EGFP-F spot. (*c*) Representative trajectories of EGFP-F moving with small (*red*) and typical (*black*) diffusion constants on the plasma membrane. Bar represents 1 μm. (*d*) Histogram of diffusion constants of EGFP-F spots measured by single-molecule tracking.

also carried out confocal FCS of EGFP-F in COS7 cells ($n = 47$ measurements). The results were $D_1 = 3.0 \pm 1.8 \times 10^{-7}$ cm^2/s, $F_1 = 50 \pm 18\%$, $D_2 = 5.9 \pm 2.6 \times 10^{-9}$ cm^2/s, and $F_2 = 50 \pm 18\%$.

DISCUSSION

TIR-FCS detection volume

Although the radius of the excitation area was ~10 μm, the TIR-FCS detection area was much smaller. The values h and ω_{xy} of the TIR-FCS observation volume were estimated by both fitting of TIR-FCS data on fluorescein in Tris-buffer solution and using the diffusion constant value of $D = 3.0 \times 10^{-6}$ cm^2/s as a standard value (Fig. 2 *a*). With the larger incident-angle of the excitation laser, which produced a thinner evanescent field, the value of h decreased, while ω_{xy} was not changed.

In the case of cellular experiments, the size of the observation volume is presumed to be a little different from that in aqueous solution measurements. Indeed, h, but not ω_{xy}, would be larger because of the higher refractive indexes of cytosol. However, we used the same value of h as for in vitro experiments, because exact estimation of the observation volume in cellular applications seems to be very difficult due to heterogeneous attachment of the plasma membrane to the glass surface. The value of h numerically calculated by MDEs (20) may be appropriate for the cellular experiments to more precisely calculate three-dimensional diffusion constants. In this study, however, the procedure to estimate observation volume used in Fig. 2 *a* should have been

sufficient to calculate the two-dimensional diffusion constants on the cell surface we were interested in.

TIR-FCS of R18 in the plasma membrane

The fitting results with the two-component model of two-dimensional diffusion, but not with the one-component model, agreed well with the measured correlation function in TIR-FCS of R18 in cell membranes (Fig. 4). This may be due to binding processes of R18 to the membrane, micellar structure, or anomalous diffusion (22). Confocal FCS also detected two diffusing species of R18 in the cell membrane (Supplementary Material, Fig. S1). A more appropriate laser wavelength (HeNe 543 nm) was used for R18 dyes (absorption maximum 556 nm) in confocal FCS, whereas our TIR-FCS system employed only a 488-nm laser in all the experiments. That is the reason why the signal bursts, as shown in confocal FCS measurements of R18, could not be observed in TIR-FCS. Nor could we do experiments using different laser powers with R18 in the cell membrane since the maximum power of the 488-nm laser only evoked weak excitation of R18, so the laser power could not be reduced.

Diffusion constants measured by TIR-FCS

Confocal FCS measurements ($D_1 = 2.7 \times 10^{-7}$ cm^2/s) confirmed that D_1 (1.1×10^{-7} cm^2/s), measured by TIR-FCS, represented free diffusion of EGFP-F located near the plasma membrane in cytosol of HeLa cells (Table 2). D_2 (5.6×10^{-9} cm^2/s) obtained by TIR-FCS was consistent with single-molecule tracking (SMT) data (4.7×10^{-9} cm^2/s) and previous research in tsA201 cells at 22°C (SMT: 5.3×10^{-9}
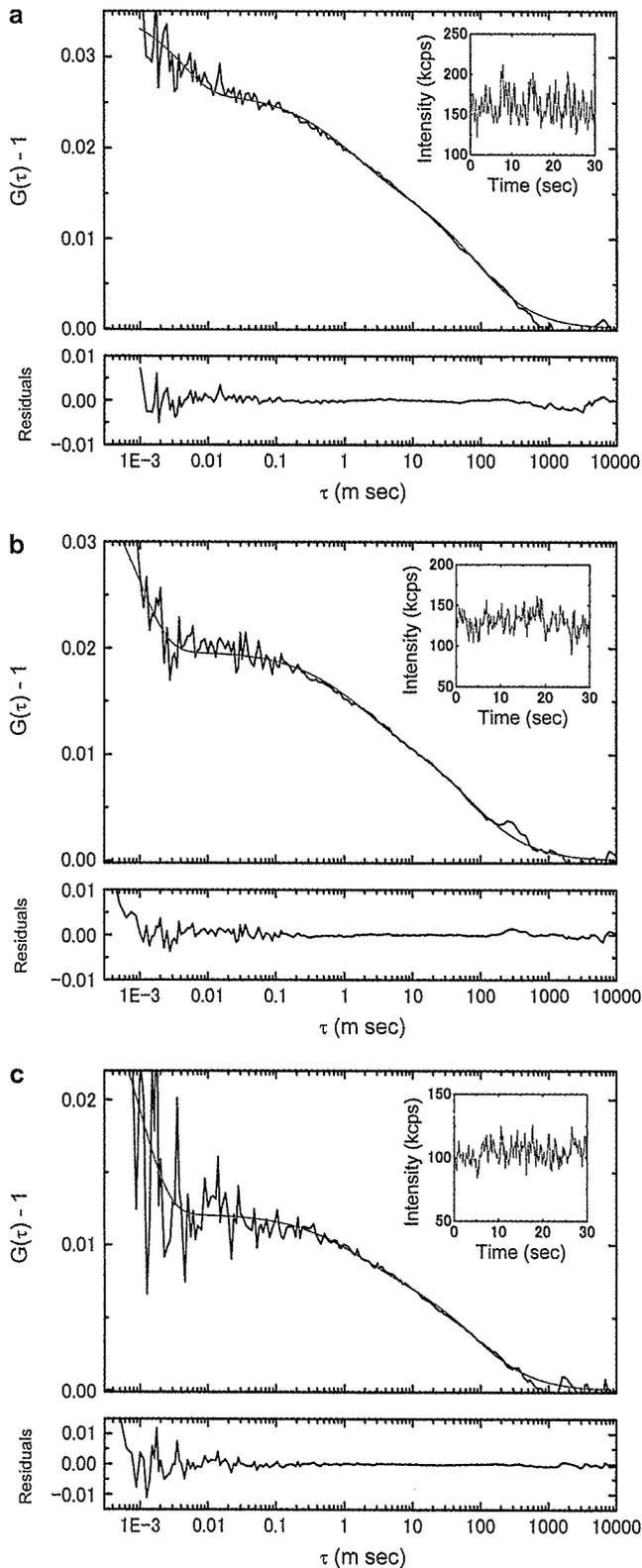
cm^2/s, FRAP: 4.8×10^{-9} cm^2/s (29)). However, the immobile fraction (0.6×10^{-9} cm^2/s (29)) detected by previous research was not observed by TIR-FCS in this study. This suggested that the minimum detectable diffusion constant of TIR-FCS was $\sim 10^{-9}$ cm^2/s, and was due to photobleaching.

The value D_1 of EGFP-F in Fig. 5 seems to be a little smaller than the value of D_1 measured by confocal FCS (Table 2). This might be due to underestimation of h (see TIR-FCS Detection Volume, above) or some interaction of EGFP-F with the cell surface.

Fraction of slow mobility on the cell surface

Although confocal FCS could detect both membrane-bound and free fluorescent molecules near the plasma membrane (Table 2), the standard deviations of the diffusion constants for the slow and fast moving components were much larger than those obtained by TIR-FCS. By using the confocal FCS, the plasma membrane can be detected very easily because the thickness of plasma membrane is only ~ 10 nm and the length of the confocal element of FCS is ~ 1 μm. However, detection of stable emission intensity from plasma-membrane-bound fluorophores may be difficult by using the confocal element of confocal FCS, because the distribution of excitation energy is changed according to the optical axis by moving the focal position. This suggests that local observation of the plasma membrane of the living cell is constantly achieved by TIR-FCS, because the thickness of the excitation field of TIR-FCS is constant at the plasma membrane. However, the detection efficiency decays much more in the axial direction in TIR-FCS. Therefore, we measured the strongest fluorescence intensity in cells whose membranes were tightly attached to the glass surface and did not undergo axial movement in and out of the exponentially decaying detection volume. However, it is necessary to design control experiments using a fluorescent probe residing exclusively in the cellular or an artificial membrane to address the possibility that minute movements of membranes in the axial direction contribute to the fluorescence fluctuation. Moreover, the dependence of diffusion times on the laser power and pinhole size should be checked in the near future as in a previous study (20). One should recognize the similarity between the TIR-FCS curve of eGFP sticking to a noncoated coverslip (Fig. 2 b, $open\ circles$) and the TIR-FCS curves of the membrane probes (Fig. 4, $black\ line$).

Although EGFP-F signals in the plasma membranes of HeLa cells were stronger than in cytosol as shown in the fluorescence microscope image (Fig. 5 b), the average

FIGURE 7 Autocorrelation functions of EGFP-F expressed in living COS7 cells with a series of laser powers. Autocorrelation functions of EGFP-F in COS7 cells by using a series of laser powers: 1.0, 0.5, and 0.25 μW/μm^2 are shown in a, b, and c, respectively. Autocorrelation functions ($black\ line$) were fitted with Eq. 3 ($red\ line$). The results were $D_1 = 0.6 \times$ 10^{-7} cm^2/s (46%) and $D_2 = 3.1 \times 10^{-9}$ cm^2/s (54%) in panel a, $D_1 = 0.5 \times$ 10^{-7} cm^2/s (46%) and $D_2 = 3.5 \times 10^{-9}$ cm^2/s (54%) in panel b and $D_1 =$ 0.4×10^{-7} cm^2/s (41%) and $D_2 = 3.5 \times 10^{-9}$ cm^2/s (59%) in panel c. The insets and the bottom panels show the fluorescence intensities and the fit residues, respectively.

TABLE 3 The relationship between TIR-FCS results and laser excitation power

	Laser power $(\mu W/\mu m^2)$	Fast		Slow	
		D_1 (cm^2/s)	F_1 (%)	D_2 (cm^2/s)	F_2 (%)
TIR-FCS	1.0	$0.7 \pm 0.2 \times 10^{-7}$	52 ± 6	$4.7 \pm 2.6 \times 10^{-9}$	48 ± 6
	0.5	$0.6 \pm 0.3 \times 10^{-7}$	51 ± 7	$4.6 \pm 2.5 \times 10^{-9}$	49 ± 7
	0.25	$0.5 \pm 0.3 \times 10^{-7}$	47 ± 10	$5.1 \pm 2.9 \times 10^{-9}$	53 ± 10

TIR-FCS of EGFP-F in COS7 cells with a series of laser excitation powers. The statistical data are based on TIR-FCS results for the same cells ($n = 14$ cells). Means $\pm$ SD.

fraction of membrane-binding EGFP-F (28%) was smaller than that of cytosol-localized EGFP-F (72%) (Fig. 5 e). This was because the depth of the evanescent field (200 nm) was still thicker than the plasma membrane (10 nm). A higher numerical aperture objective lens (NA = 1.65), which can produce a thinner evanescent field, could be expected to decrease the interference from cytosol. The fraction of F_1 measured in confocal FCS was smaller than that in TIR-FCS (Table 2). In the confocal FCS measurements, most of the area focused on by the confocal element might be off the cell. In Table 3, however, the fraction of the membrane-binding component (F_2) with laser power density 0.25 $\mu W/\mu m^2$ was 53%, which was larger than the F_2 (50%) obtained by confocal FCS of EGFP-F in COS7 cells.

The effect of photobleaching

We could measure the diffusion of EGFP near the cell surface in cytosol of HeLa cells only when using a deeper evanescent field than that used in Fig. 2 (Fig. 3). Indeed, although the autocorrelation function of EGFP in cytosol was obtained using the same incident angle for the laser as in Fig. 2, FCS signals were too weak to be analyzed by fitting. On the other hand, both cytosol-localized and membrane-anchoring EGFP-Fs were clearly detected using the same conditions of TIR illumination (Fig. 5 d). This might have been due to the interaction of EGFP-F with the plasma membrane, but it could not be explained in detail, so further study is required. However, Figs. 3–5 demonstrate that TIR-FCS was at least appropriate for monitoring of membrane-binding molecules, though not cytosol-localized molecules. Due to the reduced photobleaching by the thinner evanescent field, signal collection was performed for a longer time (30~90 s). Indeed, 30-s collection gave correlation curves clear enough for fitting (Fig. 7).

The decrease of fluorescence occurring when the cells were first illuminated might correspond to the photobleaching of the mostly immobile fraction (29) or the aggregation of EGFP-F in the plasma membranes of HeLa cells (Fig. 5).

The total number of EGFPs in a cultured cell was much smaller than that in the buffer solution for in vitro experiments, because the volume of a cell is much smaller than the total volume in an in vitro experiment. The few EGFPs in cell space were destroyed readily by the evanescent field. Thus, in cellular experiments with an incident laser-beam

angle of <70°, strong photobleaching interfered with signal collection of FCS for a longer time (Fig. 3).

After modification by double palmitoylation and single farnesylation, EGFP-F might come from the cytosol pool and then anchor in the plasma membrane like H-Ras. However, in this study, we presumed that association and dissociation of EGFP-F with the plasma membrane would rarely occur within the TIR-FCS detection volume. Since EGFP-F has two palmitoyl groups, its residence time at the plasma membrane should be longer than for membrane-anchored proteins with a single palmitoyl group like N-Ras (28). The slow process observed here may arise from EGFP-F molecules that have diffused three-dimensionally from the cytoplasm to the plasma membrane, instead of laterally within the plasma membrane into the detection volume (18,30). Detailed simulation experiments could resolve this question. However, that is beyond the scope of this article.

The assumption that diffusion constants may represent artifacts of photobleaching, but not real diffusional mobility, was denied by the experiments with a series of laser powers (Fig. 7). If D_2 represents photobleaching dynamics, the D_2 value would become smaller with weaker laser power. However, this effect did not occur (Table 3).

The disadvantage of TIR-FCS is that the total power of the laser used for illumination of the specimen is stronger than that in confocal FCS. Therefore, the fluorophores in the overall specimen, but not the detection volume, may be more easily bleached than in confocal FCS, in which the total power is lower and the excitation area is smaller. However, this weak point of TIR-FCS may be improved by a reduction of the illumination area in the x,y plane with a smaller field diaphragm.

On the other hand, the laser power density (the value obtained by division of total laser power by the illumination area), but not total power, is ~50 times lower than that in confocal FCS. This advantage of TIR-FCS may yield a smaller possibility of photobleaching artifacts, compared to confocal FCS.

Incident laser intensity of ~1 $\mu W/\mu m^2$, which was measured through the objective ($\theta = 0°$, epi-illumination), was used for TIR-FCS. This was ~50 times weaker than that for confocal FCS, suggesting that there was little possibility of photobleaching in the detection volume on the cell surface and the usefulness of dual-color TIR-fluorescence cross-correlation spectroscopy (TIR-FCCS) application in combination with both EGFP-fused proteins and photochemically unstable monomeric red fluorescent proteins.

Finally, we conclude that TIR-FCS simultaneously detects membrane-bound movement and free movement of protein in cytosol in the living cell. In the near future, we plan to employ TIR-FCS to examine the dynamic processes of proteins that undergo localization changes between the cytosol and plasma membrane (PKC, MAPKKKs, etc.). Furthermore, TIR-FCCS should be useful as a method with high sensitivity for detecting weak pairs (31) or a leading method for monitoring of protein-protein associations on the surfaces of living cells (30). Our future goal is to develop TIR-FCCS and then to employ the technique for identification and characterization of ligand-receptor or protein-protein interactions at the plasma membranes in living cells.

SUPPLEMENTARY MATERIAL

An online supplement to this article can be found by visiting BJ Online at http://www.biophysj.org.

REFERENCES

1. Rigler, R., Ü. Mets, J. Widengren, and P. Kask. 1993. Fluorescence correlation spectroscopy with high count rate and low background: analysis of translational diffusion. *Eur. Biophys. J.* 22:169–175.

2. Kinjo, M., and R. Rigler. 1995. Ultrasensitive hybridization analysis using fluorescence correlation spectroscopy. *Nucleic Acids Res.* 23:1795–1799.

3. Kinjo, M., G. Nishimura, T. Koyama, and Ü. Mets. 1998. Single-molecule analysis of restriction DNA fragments using fluorescence correlation spectroscopy. *Anal. Biochem.* 260:166–172.

4. Takakuwa, Y., C.-G. Pack, X.-L. An, S. Manno, E. Ito, and M. Kinjo. 1999. Fluorescence correlation spectroscopy analysis of the hydrophobic interactions of protein 4.1 with phosphatidyl serine liposomes. *Biophys. Chem.* 82:149–155.

5. Pack, C.-G., K. Aoki, H. Taguchi, M. Yoshida, M. Kinjo, and M. Tamura. 2000. Effect of electrostatic interactions on the binding of charged substrate to GroEL studied by highly sensitive fluorescence correlation spectroscopy. *Biochem. Biophys. Res. Commun.* 267: 300–304.

6. Nomura, Y., and M. Kinjo. 2004. Real-time monitoring of in vitro transcriptional RNA by using fluorescence correlation spectroscopy. *ChemBioChem.* 5:1701–1703.

7. Brock, R., G. Vàmosi, G. Vereb, and T. M. Jovin. 1999. Rapid characterization of green fluorescent protein fusion proteins on the molecular and cellular level by fluorescence correlation microscopy. *Proc. Natl. Acad. Sci. USA.* 96:10123–10128.

8. Terada, S., M. Kinjo, and N. Hirokawa. 2000. Oligomeric tubulin in large transporting complex is transported via kinesin in squid giant axons. *Cell.* 103:141–155.

9. Köhler, R. H., P. Schwille, W. W. Webb, and M. R. Hanson. 2000. Active protein transport through plastid tubules: velocity quantified by fluorescence correlation spectroscopy. *J. Cell Sci.* 113:3921–3930.

10. Yoshida, N., M. Kinjo, and M. Tamura. 2001. Microenvironment of endosomal aqueous phase investigated by the mobility of microparticles using fluorescence correlation spectroscopy. *Biochem. Biophys. Res. Commun.* 280:312–318.

11. Saito, K., E. Ito, Y. Takakuwa, M. Tamura, and M. Kinjo. 2003. In situ observation of mobility and anchoring of PKCβI in plasma membrane. *FEBS Lett.* 541:126–131.

12. Kamada, A., H. Nagaya, T. Tamura, M. Kinjo, H. Y. Jin, T. Yamashita, K. Jimbow, H. Kanoh, and I. Wada. 2004. Regulation of immature protein dynamics in the endoplasmic reticulum. *J. Biol. Chem.* 279: 21533–21542.

13. Haustein, E., and P. Schwille. 2004. Single-molecule spectroscopic methods. *Curr. Opin. Struct. Biol.* 14:531–540.

14. Tokunaga, M., K. Kitamura, K. Saito, A. H. Iwane, and T. Yanagida. 1997. Single molecule imaging of fluorophores and enzymatic reactions achieved by objective-type total internal reflection fluorescence microscopy. *Biochem. Biophys. Res. Commun.* 235:47–53.

15. Axelrod, D. 2001. Total internal reflection fluorescence microscopy in cell biology. *Traffic.* 2:764–774.

16. Thompson, N. L., T. P. Burghardt, and D. Axelrod. 1981. Measuring surface dynamics of biomolecules by total internal-reflection fluorescence with photobleaching recovery or correlation spectroscopy. *Biophys. J.* 33:435–454.

17. Starr, T. E., and N. L. Thompson. 2001. Total internal reflection with fluorescence correlation spectroscopy: combined surface reaction and solution diffusion. *Biophys. J.* 80:1575–1584.

18. Lieto, A. M., R. C. Cush, and N. L. Thompson. 2003. Ligand-receptor kinetics measured by total internal reflection with fluorescence correlation spectroscopy. *Biophys. J.* 85:3294–3302.

19. Hassler, K., T. Anhut, R. Rigler, M. Gösch, and T. Lasser. 2005. High count rates with total internal reflection fluorescence correlation spectroscopy. *Biophys. J.* 88:L01–L03.

20. Hassler, K., M. Leutenegger, P. Rigler, R. Rao, R. Rigler, M. Gösch, and T. Lasser. 2005. Total internal reflection fluorescence correlation spectroscopy (TIR-FCS) with low background and high count-rate per molecule. *Opt. Express.* 13:7415–7423.

21. Madin, K., T. Sawasaki, T. Ogasawara, and Y. Endo. 2000. A highly efficient and robust cell-free protein synthesis system prepared from wheat embryos: plants apparently contain a suicide system directed at ribosomes. *Proc. Natl. Acad. Sci. USA.* 97:559–564.

22. Schwille, P., J. Korlach, and W. W. Webb. 1999. Fluorescence correlation spectroscopy with single-molecule sensitivity on cell and model membranes. *Cytometry.* 36:176–182.

23. Kusumi, A., Y. Sako, and M. Yamamoto. 1993. Confined lateral diffusion of membrane receptors as studied by single particle tracking (nanovid microscopy). Effects of calcium-induced differentiation in cultured epithelial cells. *Biophys. J.* 65:2021–2040.

24. Saxton, M. J., and K. Jacobson. 1997. Single-particle tracking: applications to membrane dynamics. *Annu. Rev. Biophys. Biomol. Struct.* 26:373–399.

25. Chen, Y., J. D. Müller, Q. Ruan, and E. Gratton. 2002. Molecular brightness characterization of EGFP in vivo by fluorescence fluctuation spectroscopy. *Biophys. J.* 82:133–144.

26. Starr, T. E., and N. L. Thompson. 2002. Local diffusion and concentration of IgG near planar membranes: measurement by total internal reflection with fluorescence correlation spectroscopy. *J. Phys. Chem. B.* 106:2365–2371.

27. Parton, R. G., and J. F. Hancock. 2004. Lipid rafts and plasma membrane microorganization: insights from Ras. *Trends Cell Biol.* 14:141–147.

28. Meder, D., and K. Simons. 2005. Ras on the roundabout. *Science.* 307:1731–1733.

29. Lommerse, P. H., G. A. Blab, L. Cognet, G. S. Harms, B. E. Snaar-Jagalska, H. P. Spaink, and T. Schmidt. 2004. Single-molecule imaging of the H-ras membrane-anchor reveals domains in the cytoplasmic leaflet of the cell membrane. *Biophys. J.* 86:609–616.

30. Schwille, P. 2003. TIR-FCS: staying on the surface can sometimes be better. *Biophys. J.* 85:2783–2784.

31. Laurence, T. A., and S. Weiss. 2003. How to detect weak pairs. *Science.* 299:667–668.

nature
cell biology

Cytosolic chaperonin prevents polyglutamine toxicity with altering the aggregation state

Akira Kitamura[1], Hiroshi Kubota[1,6], Chan-Gi Pack[2], Gen Matsumoto[3], Shoshiro Hirayama[1], Yasuo Takahashi[2,4], Hiroshi Kimura[5], Masataka Kinjo[2], Richard I. Morimoto[3] and Kazuhiro Nagata[1]

Polyglutamine (polyQ)-expansion proteins cause neurodegenerative disorders including Huntington's disease, Kennedy's disease and various ataxias. The cytotoxicity of these proteins is associated with the formation of aggregates or other conformationally toxic species. Here, we show that the cytosolic chaperonin CCT (also known as TRiC) can alter the course of aggregation and cytotoxicity of huntingtin (Htt)–polyQ proteins in mammalian cells. Disruption of the CCT complex by RNAi-mediated knockdown enhanced Htt–polyQ aggregate formation and cellular toxicity. Analysis of the aggregation states of the Htt–polyQ proteins by fluorescence correlation spectroscopy revealed that CCT depletion results in the appearance of soluble Htt–polyQ aggregates. Similarly, overexpression of all eight subunits of CCT suppressed Htt aggregation and neuronal cell death. These results indicate that CCT has an essential role in protecting against the cytotoxicity of polyQ proteins by affecting the course of aggregation.

Proteins with expanded polyQ repeats are associated with at least nine neurodegenerative disorders including ataxins 1 and 3, Kennedy's disease, and Huntington's disease[1,2]. These diseases are dominantly inherited and although the polyQ-containing proteins are expressed widely in the brain, they result in selective neuronal death. There is a significant and striking correlation between the length of the polyQ repeat and pathology; longer repeats result in earlier onset and more severe symptoms with the threshold of approximately 40 glutamine residues. In the case of Huntington's disease, for example, expanded polyQ in huntingtin (Htt) protein causes disease[3,4]. A characteristic of the polyQ diseases is the appearance of neuronal inclusions that are formed by aggregation of the polyQ proteins with other cellular proteins[5,6]. This has led to the 'toxic gain-of-function' hypothesis that proposes that essential proteins can be sequestered, which over time leads to cellular dysgenesis. The expression of polyQ can cause other metastable proteins to lose functionality, and in turn these proteins amplify the toxicity of polyQ by enhancing overall aggregation[7]. Self-aggregation of polyQ proteins has been proposed to be mediated by association of parallel β-sheet structures[8]. However, the intrinsic *in vivo* events leading to the aggregation of polyQ proteins remain poorly understood.

Protein misfolding is a natural consequence of protein biogenesis. To combat cytotoxicity resulting from the accumulation of misfolded proteins, all cells express molecular chaperones that are essential for the productive folding of proteins[9,10]. Molecular chaperones are of several classes; for example, Hsp70/J-domain proteins interact with unfolded or partially folded proteins in concert with co-chaperones, whereas the chaperone machines of the chaperonin (Hsp60) family form cage-like structures that sequester non-native states of proteins[11]. CCT is a member of the chaperonin family[12] that facilitates the folding of proteins in the eukaryotic cytosol on ATP hydrolysis[13,14]. CCT shows a weak but significant homology to *Eschericia coli* GroEL and forms a hexadecamer double-troidal complex composed of eight different subunits[15,16]. Substrate proteins are captured in the cavity and released after folding is completed[17]. Approximately 10% of newly synthesized proteins have been proposed to be recognized by CCT.

In a recent genome-wide screen to identify modifier genes for polyQ aggregation in *Caenorhabditis elegans*, approximately 200 genes were found to be required for the prevention of polyQ aggregation[18]. These included the genes encoding two Hsp70s, one J-protein and six CCT subunits. These observations suggested a role for CCT in preventing polyQ aggregation. Here, we show that CCT has a key protective role against the toxicity of Htt–polyQ in mammalian cells and affects the aggregation process at the soluble stage. In the context of our recent *in vitro* data showing that CCT prevents aggregation of the trimeric G protein β subunit (Gβ) by recognizing hydrophobic β-strands[19], we discuss possible mechanisms for the CCT-dependent prevention of polyQ aggregation.
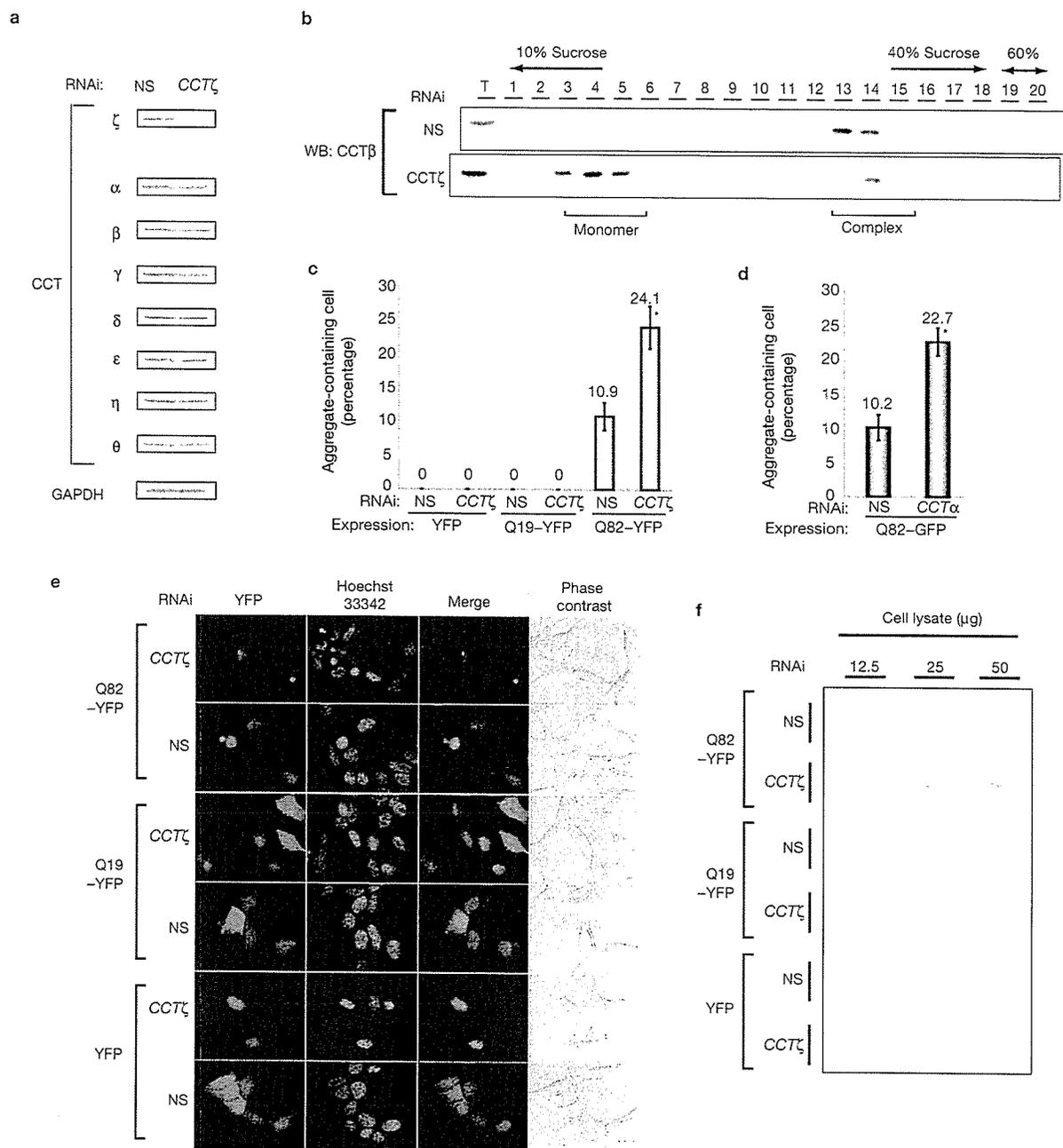
Figure 1 Knockdown of CCT subunits stimulates aggregate formation of expanded polyQ repeats transiently expressed in HEK293 cells. (a) Knockdown of the CCTζ subunit of CCT. Cells were transiently transfected with CCTζ RNAi vector or nonspecific RNAi vector (NS) as a control. Cellular proteins were extracted after 72 h and analysed by western blotting using antibodies against individual subunits. (b) The CCT complex is disrupted by CCTζ knockdown. Proteins extracted from CCTζ RNAi-treated cells or untreated cells were fractionated by sucrose gradient centrifugation. Fractions were analysed by western blotting using anti-CCTβ antibody. (c) CCTζ depletion increases number of cells containing Q82-YFP aggregates. Cells were transfected with polyQ expression vector (Q82-YFP, Q19-YFP or YFP alone) in the presence of CCTζ RNAi or non-specific RNAi vectors. Number of cells showing YFP fluorescence with or without aggregates were counted and the percentage of aggregate-positive cells were calculated (n = 3). (d) Q82-GFP aggregation is stimulated by RNAi knockdown of CCTα. (n = 3) (e) Fluorescent microscopic images of polyQ-YFP expressed in HEK293 cells treated with CCTζ RNAi or non-specific RNAi vectors. Scale bar represents 20 µm. (f) Filter-trap assay of polyQ-YFP aggregates. Cell lysates containing indicated amount of protein were filtered on cellulose acetate membranes and polyQ-YFP aggregates were detected by immunoblotting using anti-YFP antibody. The asterisks indicate P 0.01; Student's t test. The error bars in c and d represent s.d.

To address whether CCT has a direct role in polyQ aggregation and toxicity, the levels of CCT in human tissue culture cells were depleted using an RNA interference (RNAi)-mediated CCT subunit knockdown system. HEK293 cells were transiently transfected with a CCTζ small interfering RNA (siRNA) expression vector or a non-specific siRNA vector as a control, and the levels of CCT subunits were examined by western blot analysis (Fig. 1a and see Supplementary Information, Fig. S5). The level of CCTζ was reduced by more than 75%, indicating efficient